Brumand-Poor *et al. Advanced Modeling and Simulation in Engineering Sciences(2025)12:2*
https://doi.org/10.1186/s40323-025-00283-9

Advanced Modeling and Simulation in Engineering Sciences

RESEARCH ARTICLE Open Access

Extrapolation of cavitation and hydrodynamic pressure in lubricated contacts: a physics-informed neural network approach

Faras Brumand-Poor[†], Freddy Kokou Azanledji[†], Nils Plückhahn, Florian Barlog, Lukas Boden and Katharina Schmitz

[†]Faras Brumand-Poor and Freddy Kokou Azanledji contributed equally to this work.

[*]Correspondence: faras.brumand@ifas.rwth-aachen.de

[1]RWTH Aachen University, Institute for Fluid Power Drives and Systems (ifas), Campus-Boulevard 30, Aachen 52074, Germany

Abstract

A comprehensive understanding of the dynamics of tribological interactions is essential for enhancing efficiency and durability in a multitude of technical domains. Conventional experimental techniques in tribology are frequently costly and time-consuming. In contrast, elastohydrodynamic lubrication (EHL) simulation models present a viable alternative for calculating frictional forces in sealing contacts. These calculations are based on the hydrodynamics within the sealing contact, as defined by the Reynolds equation, the deformation of the seal, and the contact mechanics. However, a significant drawback of these simulations is the time-consuming calculation process. To overcome these experimental and computational limitations, machine learning algorithms offer a promising solution. Physics-informed machine learning (PIML) improves on traditional data-driven models by incorporating physical principles. In particular, physics-informed neural networks (PINNs) are as effective hybrid solvers that combine data-driven and physics-based methods to solve the partial differential equations that drive EHL simulations. By integrating physical laws into the parameter optimization of the neural network (NN), PINNs provide accurate and fast solutions. Thus, unlike traditional NNs, PINNs have the potential to make accurate predictions beyond the limited training domain. The objective of this study is to demonstrate the feasibility of spatial and temporal extrapolation of the PINN and to analyze its reliability, both with and without consideration of cavitation. Two test cases are employed to examine the pressure and cavitation distribution within a sealing contact that extends beyond the spatial and temporal training range. The findings indicate that PINNs can surmount the typical constraints associated with NNs in the extrapolation of solution spaces, which represents a notable advancement in terms of computational efficiency and model flexibility.

Keywords: Cavitation extrapolation, Elastohydrodynamic lubrication simulation, Hydrodynamic pressure extrapolation, Physics-informed machine learning, Physics-informed neural networks, Pneumatic sealing, Spatial and temporal extrapolation, Tribology

Introduction

Mechanical components in technical systems rely heavily on the performance of their lubricated tribological contacts, such as those in seals, which play a vital role in ensuring efficiency, durability, and functionality. Seals are indispensable in numerous engineering applications, and their failure can lead to significant operational disruptions, costly repairs, and, in extreme cases, catastrophic outcomes. Elastomeric seals, including O-rings, X-rings, and rectangular rings, are widely utilized for their cost-effectiveness and simplicity [1]. However, replacing these seals can involve complex, time-intensive, and expensive processes. Seals are essential for maintaining the pressure required for system operation in fluid power systems. Nevertheless, dynamic seals generate friction during use, diminishing system performance and efficiency. This issue is particularly critical in valves, where even small frictional forces can adversely affect valve dynamics and downstream components. Despite decades of industrial use, particularly in pneumatic systems, the frictional mechanisms in pneumatic sealing contacts still need to be more understood. A typical dynamic sealing system, such as in pneumatic applications, consists of key elements: the seal, the housing, the cylinder, and the lubricant. The contact interface, often involving a rigid counter surface such as a moving cylinder, operates within a hydrodynamic lubrication regime where the gap is partially or completely filled with lubricant. Understanding these lubricated contacts is a complex task due to the interplay of fluid dynamics, contact mechanics, and material properties. Dynamic friction, mainly driven by fluid behavior, is crucial in accurately modeling these systems. Simplifications in analytical models can compromise accuracy, while experimental studies are often resource-intensive and costly. One of the most effective approaches to studying these interactions is through elastohydrodynamic lubrication (EHL) simulations. EHL employs the Reynolds equation to model pressure distribution and deformation in the contact region, offering a robust framework for understanding and optimizing tribological systems. However, the intricate nature of these phenomena often demands advanced simulation techniques to capture the full range of behaviors observed in dynamic sealing systems.

A widely used method for solving EHL problems involves numerical approaches [1–3]. One such approach is fluid–structure interaction (FSI), which couples the deformation of the solid structure, determined through Finite Element Analysis (FEA), with the hydrodynamic behavior of the lubricant [4,5]. Another common technique is Model Order Reduction (MOR), which employs hyper-reduction algorithms to project the problem onto a low-dimensional subspace. This method significantly reduces computational effort while maintaining solution accuracy [6]. In addition to numerical methods, research has also been conducted to derive analytical solutions for EHL problems [7,8]. These analytical model focus on specific parts of the EHL problem, by either simplifying the underlying equations or developing an analytical solution for a particular part of the whole model. Beyond numerical and analytical approaches, experimental studies have played a significant role in understanding EHL phenomena, with research dating back to the 1950 s. Early studies focused on predicting film thickness in lubricated rollers [9]. A prominent experimental technique is optical EHL, which allows for the direct observation of lubricant films and is often used to validate analytical models [10,11]. Another experimental approach involves attaching sensitive pressure and capacitance transducers to one of the interacting surfaces to measure key parameters [12].

A monolitic EHL simulation model was developed at the Institute for Fluid Power Drives and Systems (ifas) at RWTH Aachen University to investigate reciprocating seals in pneumatic valves [13–16]. This model, designated ifas DDS (Dynamic Description of Sealings), is utilized to ascertain the degree of friction by resolving the hydrodynamic interactions within the sealing contact. The model considers both contact mechanics and seal deformation [17]. Prior research has validated this model using experimental data [18]. Compared to the previously mentioned EHL simulations, the ifas DDS does not rely on fluid–structure interaction. Moreover, the model is implemented monolithically, meaning that deformation and hydrodynamics are solved simultaneously. However, the extensive computational time required to solve the equations using numerical methods is a significant limitation. While increasing computational resources can be beneficial, it is not always feasible, particularly when the complexity of the simulations increases and real-time calculations are necessary for applications such as control systems. An accelerated approach for modeling EHL simulations, particularly for the ifas DDS, has been developed using machine learning techniques to address these challenges. This approach has been explored in prior studies, where the EHL problem was systematically modeled step by step [19–24].

Employing machine learning algorithms, including neural networks (NNs), is a promising alternative to traditional EHL simulations [25–27] and has been already implemented successfully for EHL line contacts in cylindrical roller bearings [28,29]. This is due to the rapid computation capabilities that can be achieved post-training. However, conventional NNs typically fail to incorporate the underlying physical principles. The primary objective of regression tasks is to minimize the discrepancy between the predicted and actual values. This data-driven approach is contingent upon the availability of a sufficient quantity of data, as insufficient data may result in underfitting, whereby the NN cannot accurately capture the correlations. Conversely, excess data may lead to overfitting, which can result in elevated error rates with new data points, particularly those that fall outside the training domain.

Physics-informed neural networks (PINNs) represent a significant advancement in this field, as they incorporate physical laws into the training process. PINNs represent a class of machine learning solvers for partial differential equations (PDEs). Their training process incorporates physical equations described by the initial (IC) and boundary conditions (BC), as well as the residuals of the PDEs. In contrast to conventional NNs, this enables them to enhance prediction accuracy and extend their applicability beyond the scope of the training domain.

PINNs have been used effectively in tribology, particularly for tasks such as predicting lubricant behaviour and assessing wear and damage [30,31]. Compared to MOR techniques in EHL simulations [6], PINNs offer notable advantages, such as flexibility in incorporating new parameters or modifying architectures to suit specific problems. They are particularly adept at handling discontinuities, such as cavitation with zero-pressure regions, which pose challenges for MOR approaches, including the Reduced Basis method. In addition, PINNs enable faster computation once training is complete, making them a practical choice for dynamic EHL scenarios. In particular, the potential to predict reliable values beyond the parameters of the training domain represents a significant advantage when investigating tribological problems. This capacity provides the opportunity to gain insight into system areas where direct measurements are not feasible. In numerous

real-world applications, conditions are perpetually evolving. A model that is capable of extrapolation is more resilient to unforeseen or novel scenarios. In contrast, traditional simulation models are typically unable to perform such extrapolation, necessitating a repetitive, time-consuming numerical calculation across the entire geometry of the seal. In the context of machine learning, extrapolation refers to the prediction or estimation of values for input points that lie outside the range covered by the training points. In other words, the model attempts to apply patterns or relationships to input points that go beyond the limits of what it saw during training. In contrast to extrapolation, interpolation refers to the prediction or estimation of values for input points that lie within the range covered by the training data. These are input values that fall within the range of values that the model has learned during training.

Several studies on PINNs have focused on the hydrodynamic aspect of EHL simulations, excluding deformation and friction. Furthermore, previous work has demonstrated the effectiveness of PINNs on the hydrodynamic aspect only in the interpolation domain. Almqvist was among the pioneers in applying PINNs to study pressure distribution governed by a simplified one-dimensional variant of the Reynolds equation [32]. Subsequently, Li and colleagues broadened the application of PINNs to encompass the two-dimensional Reynolds equation, particularly in the context of gas bearings [33]. Subsequent advancements were made by Yadav et al., who applied PINNs to analyze journal bearings [34], and Zhao et al., who explored the utility of PINNs in modeling linear sliders [35]. A noteworthy contribution by Rom introduced a successful approach for solving the Reynolds equation integrated with the Jakobsson-Floberg-Olsson (JFO) cavitation model [36]. His methodology involved the implementation of soft constraints and a dynamic adaptation of collocation points, which enabled the accurate representation of cavitation zones and regions with steep gradients. Building on this, Cheng and colleagues extended the PINN framework to incorporate the JFO and Swift-Stieber (SS) cavitation models [37].

In recent developments, Xi et al. proposed an improved PINN strategy for solving the Reynolds equation. This strategy employs a combination of hard and soft constraints during training, which has been shown to enhance the accuracy of the solution [38,39]. Brumand-Poor et al. developed a hydrodynamic lubrication framework for solving the transient Reynolds equation in scenarios with and without cavitation for one-dimensional sealing gaps. Furthermore, Brumand-Poor et al. addressed challenges related to interpolation and extrapolation, as documented in several publications [19–24]. Rimon et al. investigated the application of PINNs to an EHL model. Their approach combined a simplified stationary Reynolds equation, excluding cavitation, with the Lamé equation to account for seal deformation [40]. The previously mentioned research has focused on the use of purely physics-based PINNs. However, investigations have also been conducted on hybrid PINNs for hydrodynamic lubrication by incorporating a data-based loss. Shutin et al. were the first to explore this approach for determining the hydrodynamic behavior of fluid films in journal bearings [41]. Similarly, Zhao et al. applied hybrid PINNs to model lubrication in slider bearings [42]. Another application of PINNs in the context of hydrodynamic lubrication was conducted by Xi et al., who addressed the inverse problem of the Reynolds equation by integrating data into the PINN. This method solved the Reynolds equation and determined the eccentricity and geometric parameters of a journal bearing [43].

Similar to the prior mentioned publications, this contribution also focuses on the hydrodynamic aspect of EHL, while neglecting friction and contact mechanics. Deformation is artificially modeled by a constant seal movement, which ignores pressure dependencies. In contrast to previous research in this area, the results presented in this paper demonstrate the efficacy of PINNs in spatio-temporal extrapolation tasks. A hydrodynamic-PINN (HD-PINN) framework, previously implemented and validated for stationary scenarios without cavitation [19], has been demonstrated to permit extrapolation tasks of the pressure distribution beyond the boundaries of the trained regimes [20]. As further research, this framework is extended to enable the modeling of the Reynolds equation, incorporating sliding and squeezing motions as well as cavitation effects, which are observed in sealing contacts. This contribution demonstrates the feasibility of spatial and temporal extrapolation of the extended HD-PINN framework across spatial and temporal boundaries. Extrapolating pressure distribution and cavitation effects in tribological systems are beneficial, as predictions, especially temporal ones, beyond the training domain provide valuable information for modeling and understanding these systems (e.g., the development of cavitation regimes inside the sealing gap). Additionally, the computation time, which includes both training and evaluation phases, can be reduced since training is not required for the entire spatial and temporal domain.

Methods

This section provides a detailed description of the methods used to address and solve problems in the field of lubricated tribological contacts. Hydrodynamic lubrication, a fundamental aspect of many lubricated tribological contacts, is usually described by the Reynolds equation. The conventional numerical approach to solving this equation is presented first. Subsequently, the potential for a more innovative approach to solving the Reynolds equation with PINNs is demonstrated. The primary focus is on the ability of PINNs to extrapolate across boundaries compared to traditional numerical methods. An extended HD-PINN framework is presented, which has been expanded to include transient and cavitation terms. To demonstrate the feasibility of the spatial and temporal extrapolation capability two test cases are defined. Furthermore, a novel training procedure is presented, which is designed to enhance the extrapolation capability.

Hydrodynamic lubrication—the reynolds equation with cavitation modeling

EHL simulations are essential for the analysis of wear, friction, and leakage in lubricated mechanical interfaces. These simulations study the dynamic interactions between lubricants and contacting surfaces, focusing on the computational modeling of surface deformations and the resulting hydrodynamic pressure within the contact area. They are crucial for the design and optimization of tribological contacts in various industrial applications.

The ifas DDS model is an advanced simulation framework that has been validated against experimental data under various operating conditions [18]. This model elucidates the complex interactions between a seal and its mating surface, emphasizing the lubricating film that separates them and significantly influences seal behavior. The model uses Abaqus finite element software to accurately simulate seal deformation under operating conditions, integrating the Reynolds equation to calculate hydrodynamic phenomena

through custom user subroutines. This research focuses on solving the Reynolds equation and simplifying the model by excluding surface deformation, contact mechanics, and friction. The goal is to study lubrication aspects without the added complexity of deformations.

In order to validate the extrapolation capability of the PINN, a variant of the ifas DDS model, the so-called rigid DDS, is employed. The rigid DDS is a model that focuses exclusively on lubrication dynamics. The rigid DDS is a model that focuses exclusively on the lubrication dynamics. The two mating surfaces of the lubrication gap can move relative to each other. However, deformation, friction, and contact mechanics of the mating surfaces are not taken into account. This enables a direct comparison between the PINN solver and the rigid DDS, both of which were developed to solve the same underlying equations.

The Reynolds equation, integrated into the DDS model, is based on Osborne Reynolds' original formulation of 1886, which has been extended by the Jakobsson Floberg-Olsson (JFO) cavitation model. This introduces the cavitation fraction concept, represented by the variable θ [17]. The value of θ represents the local volume fraction of the gas phase and ranges from zero (no cavitation) to one (complete cavitation). Furthermore, the model integrates the flow factors Φ^{τ} and Φ^{p} according to the work of Patir and Cheng [44, 45]. This extension allows for the consideration of the effects of surface topography on lubrication. The extended form of the Reynolds equation is thus described as follows [17]:

$$\underbrace{\frac{v}{2}\frac{\partial}{\partial x}\Big((1-\theta)\left(R_q\Phi^{\tau}+h\right)\Big)}_{\text{Couette flow}}-\underbrace{\frac{1}{12\eta}\frac{\partial}{\partial x}\left(\Phi^{p}h^{3}\frac{\partial p}{\partial x}\right)}_{\text{Poiseuille flow}}+\underbrace{\frac{\partial}{\partial t}\Big((1-\theta)\,h\Big)}_{\text{Transient term}}=0 \tag{1}$$

The Reynolds equation describes the hydrodynamic pressure p and the cavity fraction θ in thin liquid films, considering the dynamic viscosity η, the relative velocity v between the contact surfaces, and the gap height h. This PDE plays a pivotal role in analyzing lubricated contacts with incompressible fluids. The variables of time t and location x are of particular significance in this equation, as they are essential for its formulation. Furthermore, the influence of contact surface roughness on the hydrodynamic behavior is incorporated through the parameters Φ^{τ} and Φ^{p}, which represent the shear and pressure flow factors, respectively. Additionally, the mean square roughness R_q is also included in the equation. The Fischer-Burmeister Equation, as employed by Woloszynski et al. [46], establishes the relationship between pressure and cavity fraction:

$$p+\theta-\sqrt{p^2+\theta^2}=0 \tag{2}$$

The cavity fraction provides insight into the occurrence of cavitation within the lubricated contact, which is defined as the formation of vapor when the pressure drops below the vaporization threshold, which is set to zero. The JFO cavitation model and its implementation make only minimal assumptions about the physical mechanisms, causing the cavity fraction to be non-zero. This allows it to track lubricant distribution in tribological contacts with limited lubricant supply (starved lubrication), such as grease-lubricated sealing contacts in pneumatic spool valves. In these cases, a non-zero cavity fraction indicates partial filling of the sealing gap.

In the DDS, a user-defined element (UEL) is implemented within the Abaqus finite element framework to calculate the fluid pressure and cavitation fraction in the contact zone of a seal. The UEL integrates the Reynolds equation and a cavitation model into both the Jacobian matrix and right-hand side vector to iteratively solve the nonlinear relationship between deformation variables and fluid pressure values. This approach aligns with the general finite element method (FEM) formulation $\mathbf{K} \cdot \mathbf{u} = \mathbf{RHS}$, where $\mathbf{u}$ represents the deformation vector, $\mathbf{K}$ is the stiffness matrix, and **RHS** is the right-hand side of the system of equations. The **RHS** vector encapsulates all external forces acting on the system. This includes all forces or loads that act on the nodes of the finite element model, which essentially lead to deformation in the structure. Solving the system of equations allows for the determination of the resulting deformation vector $\mathbf{u}$.

In the context of the UEL, the fluid state is characterized by pressure p and cavitation fraction θ, rather than spatial coordinates. Both the Reynolds and Fischer-Burmeister equations are structured to equal zero thus they are incorporated into **RHS** of the system of equations. The Jacobian matrix of the UEL is derived by differentiating these equations with respect to all spatial and fluid coordinates of the deformation vector $\mathbf{u}$.

By combining the element formulations for the solid and fluid domains into a single system of equations, the method enables a monolithic solution using the implicit Newton solver. Due to the axisymmetric nature of the sealing gap, combined with the negligible gap height compared to the contact length, a one-dimensional discretization using the finite difference method and solution of the Reynolds and Fischer-Burmeister equation is chosen. Through iterative adjustments of the shared "deformation" vector, the solver simultaneously resolves the solid deformation and the fluid pressure and cavitation distribution. This modeling of fluid-solid interaction is crucial for accurately predicting the operational conditions of seals, considering pressure distributions and cavitation phenomena. For validation of the Reynolds equation solution in this work, surface deformation, contact mechanics, and friction are neglected, thereby simplifying the DDS.

Physics-informed neural network

The Reynolds equation represents a fundamental mathematical tool for the modeling of pressure distribution in lubricated contacts. In the absence of an analytical solution in most cases, numerical methods such as finite volume, element, or difference approaches are typically employed to address tribological problems. However, the employment of numerical methods frequently necessitates the allocation of substantial computational resources. Consequently, the utilization of machine learning in tribology has recently demonstrated considerable promise, facilitating notable advancements [30,47]. Deep learning, particularly deep neural networks, has already shown efficacy in fault detection in tribological systems, including ball bearings, plain bearings, and slipper bearings [48–50]. One illustrative example is the contribution of Hess and Shang, who employed a convolutional neural network to calculate the elastohydrodynamic pressure distribution in plain bearings [51]. It is widely acknowledged that traditional machine learning models are characterized by their flexibility and ease of implementation. In general, these models are data-driven, or what is commonly referred to as a "black-box" model. In recent times, however, hybrid models that combine data-driven and physics-based approaches have gained considerable traction. In instances where only a limited quantity of measurement data is available,

and a comprehensive mathematical system description is lacking, models based solely on data or exclusively on physical principles (white-box modeling) are not viable [52]. In such cases, hybrid models offer a suitable alternative. Over time, various configurations of these models have been explored, including sequential, parallel, and structured forms [53–55].

In the field of tribological research, PIML represents a promising development. In PIML, machine learning models are integrated with physical principles to enhance the representation of phenomena such as friction, wear, and/or lubrication [31]. The application of such models in the field of tribology encompasses a range of applications, from the evaluation of lubrication conditions in hydrodynamic interfaces to the prediction of wear or damage. In contrast to traditional machine learning methods, which rely solely on data-driven strategies, PIMLs, especially PINNs, utilize physical principles to direct the learning process. Consequently, these models frequently yield more precise and dependable outcomes than those derived from purely data-driven methodologies. PINNs employ a NN for predictive purposes but are trained with the applicable laws of physics by including residual terms in the loss function [56].

In early work, Cybenko demonstrated that neural feed-forward networks with at least one hidden layer are capable of approximating any continuous function with a desired degree of accuracy [57]. Hornik subsequently expanded these findings to encompass measurable Borel functions [58]. The contributions to the physically based regularization of NNs by Lee [59] and Lageris [60] are based on the results of Cybenko and Hornik. Although there is no explicit reference to the term "physically-informed," the work of Lee and Lagaris is consistent with the fundamental principles underlying the development of PINNs. Lee's approach constituted an extension of the NN loss function into which pertinent differential equations were embedded, thereby establishing the foundation for PINNs. This concept had a considerable impact on subsequent developments in PIML, as it facilitated the integration of domain-specific knowledge into traditional machine learning. The integration of physical laws into the training of NNs was originally a relatively unexplored area due to limited computational resources and underdeveloped computer algebra techniques. Nevertheless, this concept has recently been revitalized as both the methods of efficient gradient computation, such as automatic differentiation, and hardware capabilities have evolved.

The revitalization of PIML was initialized by Owhadi in 2014. He was the first to integrate prior knowledge into the solution process by framing the solutions of PDEs as Bayesian inference problems, thereby enhancing algorithms with existing information [61]. Building on this foundation, Raissi and his team developed a probabilistic machine learning framework that employs Gaussian processes to solve general linear equations, with a particular focus on integro-differential equations and PDEs [62,63]. Subsequently, this methodology was extended to effectively address nonlinear PDEs [64,65].

A significant development was the advent of PINNs, which are characterized as mesh-free models that reframe the resolution of PDEs as an optimization problem defined by a loss function [66]. PINNs were introduced as a novel class of hybrid solvers with the capacity to accurately address a range of forward and inverse problems described by PDEs [67–69]. Antonello et al. expanded the PINN concept to encompass control tasks by incorporating control inputs into the network, thereby developing an algorithm capable of solving control applications [70]. PINNs process inputs such as case-dependent parameters, position x, and time t in a manner analogous to that of traditional NNs.

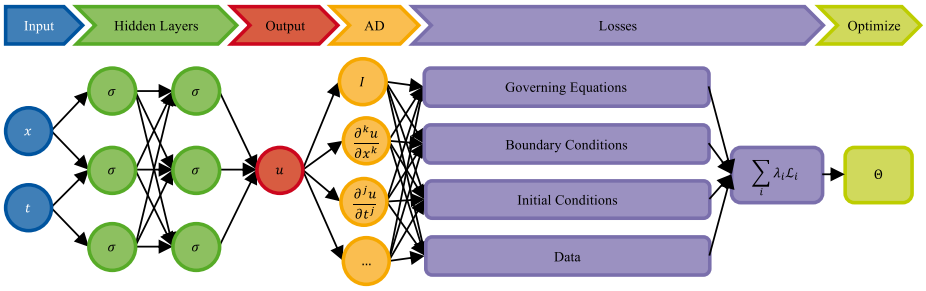

Fig. 1 Schematic illustration of a PINN [19]

The input values are processed through the hidden layers of the network, resulting in the generation of the network's output. Each neuron performs a series of mathematical operations, including the multiplication of inputs by a weight factor, the addition of a bias, and the application of an activation function σ, which collectively enable the calculation of the neuron's output. The net result of these operations is the generation of a complex function as the output of the NN.

The residual losses correspond to the residuals of the governing physical equations, making this an unsupervised loss [71]. The evaluation of loss is conducted at designated spatial and temporal junctures, referred to as collocation points. In order to integrate complex differential equations, NNs employ automatic differentiation (AD), which is capable of efficiently computing gradients of any order with machine accuracy by applying differential rules such as the chain and product rules. In conventional NNs, AD is employed for parameter updates, whereas in PINNs, it is also utilized for the calculation of derivatives $(\frac{\partial^k u}{\partial x^k}, \frac{\partial^j u}{\partial t^j}, ...)$ associated with differential equations. The objective of the losses associated with boundary conditions and ICs is to guarantee that the prescribed boundary and ICs for the partial differential equation are satisfied. The two aforementioned losses are subject to supervisory control.

Figure 1 illustrates an exemplary PINN. The network depicted is a hybrid PINN comprising physically informed and data-driven components. The available data is employed to accelerate the convergence of the governing equations, thereby facilitating the attainment of a more accurate solution. The data loss term corresponds to the classical data-driven loss. The loss terms are then each multiplied by a weight factor and added together. Subsequently, the network parameters Θ are optimized so that the weighted loss sum is minimized.

Prior to outlining the methodologies and loss functions utilized in this study, it is imperative to provide a concise overview of the applications of PINNs in the field of hydrodynamics. Subsequently, a synopsis of extant research on the extrapolation of PINNs will be provided.

Applying physics-informed neural networks to solve the Reynolds equation

The following Table 1 provides an overview of the existing literature dealing with the use of purely physics-based PINNs to solve the Reynolds equation.

Almqvist's paper can be regarded as one of the first to use PINNs to solve a simplified form of the Reynolds equation [32]. Subsequently, this approach was further developed through the development of sophisticated algorithms to solve the 2D Reynolds equation

Table 1 Summary of various NNs employed in literature for solving the Reynolds equation

Author	Inputs[1]	Layers	Layer size	Output
Almqvist [32]	x	1	10	p
Cheng et al. [37]	x, y	6	20	p
Hess et al. [51]	$h_{(x,y)}$	6	three-dim, see paper	p
Ramos et al. [72]	x, y, ϵ, α	7	(4, 12, 50, 50, 25, 12, 1)	p
	$x, y, \epsilon, \alpha, u, v$	6	(6, 15, 60, 60, 15, 1)	p
Rimon et al. [40]	x	4	30	p, Q
Rom [36]	x, y	6	20	p, θ
	x, y, e_{rel}	6	20	p, θ
Xi et al. [39]	x	3	64	p, θ
Zhao et al. [35]	x, y	2, 3 and 4	16, 32	p

[1] The notation used includes eccentricity (ϵ), angle of attack (α), velocities in the x and y directions (v and u respectively), and leakage rate (Q)

in various applications such as linear slides, gas bearings and plain bearings [33–35]. Rom made significant progress by being the first to apply PINNs to the stationary Reynolds equation, integrating the JFO cavitation model and introducing relative eccentricity as an input parameter to the PINN [36]. Extending these developments, Cheng et al. implemented a PINN that successfully solves the Reynolds equation considering the JFO or the Swift-Stieber (SS) cavitation model. The approach integrates three different multi-task learning strategies to optimize the loss components tailored to each model [37]. In another study, Xi et al. investigated the steady-state Reynolds equation with cavitation, incorporating both soft and hard constraints in the loss function to achieve higher solution accuracy [39]. Rimon et al. investigated the potential of PINNs in EHL simulation. They used a simplified Reynolds equation and modeled the seal deformation with the Lamé equation [40].

Extrapolation with physics-informed neural network

In the context of this paper, interpolation refers to the estimation of pressure and cavitation distribution within the spatial and temporal range of the training collocation points. Conversely, extrapolation pertains to the estimation of pressure and cavitation distribution beyond this range. Previous works on PINNs for solving hydrodynamic lubrication scenarios have focused on presenting their effectiveness using testing points within the interpolation domain. A promising aspect of PINNs is their capacity to extrapolate. This refers to a model's ability to generate predictions for regions that lie outside the range of the training points. Initial research on PINNs' extrapolation capabilities includes work by Kim et al., who developed an algorithm to adjust the gradient for residual and BC loss, aiming to extrapolate the solution of Burger's equation over time [73]. Fesser et al. explored transfer learning on equations like Burger and Allen-Cahn to enhance time extrapolation [74]. The research conducted by Bonfanti et al. examines the behavior of PINNs when applied to problems outside of their training domain. Using a simple 1D problem, the study analyses the effects of training hyperparameters on the extrapolation ability [75].

In the field of hydrodynamic lubrication, initial research was conducted by the authors of this paper [20]. In this work, a PINN framework was applied to solve extrapolation tasks for a simplified variant of the Reynolds equation. The results have indicated that PINNs

Table 2 The two test cases examined in this study, which are designed to assess the spatial and temporal extrapolation capabilities of the HD-PINNs

	Sealing movement[1]		**Transient cavitation** [2]	
Variable	**Value [-]**	**Gap geometry**	**Value [-]**	**Gap geometry**
		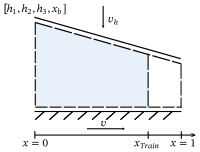		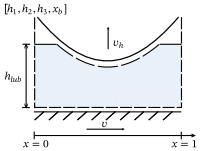
$[p_l, p_r]$	[0.5, 1.0]		[0, 0]	
$[\theta_l, \theta_r]$	[0, 0]		[0.5, 0.5]	
v	0.1		0.2	
v_h	−0.1		0.03	
h_{lub}	1.0		0.5	
$[h_1, h_2, h_3, x_b]$	[1, 0.5, 0, 0]		[1, 1, 3, 0]	

[1] $\theta = 0$, $\frac{\partial \theta}{\partial t} = 0$. In the context of the "Sealing Movement" test case, a convergent lubrication gap is considered in which the rigid seal moves in the direction of the counter surface at a constant speed v_h. The investigation of extrapolation capability here includes the prediction of the pressure distribution without cavitation, both across the positional and temporal training domains

[2] $\frac{\partial \theta}{\partial t} \neq 0$. In the context of the "Transient Cavitation" test case, a convergent-divergent lubrication gap is investigated in which the rigid seal moves away from the counter surface at a constant speed v_h. The investigation of the extrapolation capability is focused exclusively on the temporal dependency of the pressure and cavitation distribution

can not only determine the pressure distribution for a stationary convergent scenario within the interpolation range but also have the ability to extrapolate beyond the limits of this range. With regard to position extrapolation, the PINN demonstrated an aptitude for adapting to the rigid ifas DDS. When extrapolating the pressure boundaries, the single-case PINN exhibited an inability to accurately calculate the pressure distribution. In contrast, the multi-case PINN demonstrated satisfactory performance in both extrapolation and interpolation of pressure boundaries. However, the PINN faced challenges with multi-case and height-related extrapolation tasks. The present work represents an extension of the above investigations and integrates transient and cavitation terms of the Reynolds equation into the framework. The extrapolation capability of single-case PINNs is tested across positional and temporal boundaries. The subsequent section presents the HD-PINN framework, including the test cases, the PINN structure, and the training procedure that are the subject of this paper.

HD-PINN framework

This section will provide an overview of the later simulated test cases. Then it will present the NN's structure and functions.

Test cases and physics-informed loss

The present study examines two distinct test cases, as illustrated in Table 2.

In both cases, the system comprises a flat counter surface, which is moving with a constant velocity v and a rigid sealing geometry, which is described by four coefficients $[h_1, h_2, h_3, x_b]$ where $x \in [x_l, x_r]$ as follows:

$$h(x) = \begin{cases} \frac{h_1-h_2}{x_b-x_l} \cdot \mathrm{ReLU}(x_b - x) + h_2 + h_3 \left(x - \frac{x_l+x_r}{2}\right)^2 - h_3 \left(\frac{x_l+x_r}{2}\right)^2 & x_b \neq x_l \\ h_1 + (h_2 - h_1) \cdot (x - x_l) + h_3 \left(x - \frac{x_l+x_r}{2}\right)^2 - h_3 \left(\frac{x_l+x_r}{2}\right)^2 & x_b = x_l \end{cases} \tag{3}$$

In order to demonstrate the extrapolation capability in both spatial and temporal dimensions, a test domain with $x \in [0, 1]$ and $t \in [0, 1]$ is defined. The boundaries of the training domain, represented by x_{Train} and T_{Train}, are situated within the test range. They divide the test domain into an interpolation domain and an extrapolation domain. This implies that the spatial and temporal collocation points for training the PINN lie within the interval $[0, x_{Train}]$ and $[0, T_{Train}]$, whereas the test is conducted with collocation points that extend over the entire test area.

In contrast to the preceding publication, the PINN structure has undergone modification. The network has been expanded to comprise 17 inputs, including x and t, as well as all mentioned parameters and variables associated with the modified Reynolds equation. The network generates predictions for pressure p and cavitation θ. Furthermore, additional loss terms were incorporated into the HD-PINN to address both transient and cavitation issues, as illustrated in Fig. 2 and Table 3. The BCs, specifically p_l and p_r, as well as θ_l and θ_r are fixed and defined on x_l and x_r, respectively. The BCs for the pressure p at x_{Train} are provided by the DDS at every time step. The cavitation IC at $t = 0$ is determined by the lubricant film height h_{lub}. It should be noted that dynamic viscosity of the fluid η is set to one. Furthermore, shear and pressure flow factors are disregarded, with $\phi^\tau = 0$ and $\phi^p = 1$, thus assuming smooth surfaces. All other simulation parameters are presented in Table 2.

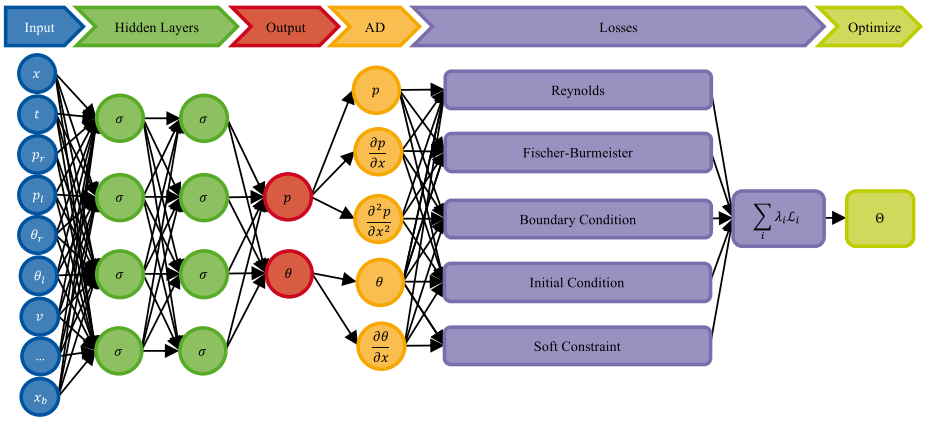

Fig. 2 HD-PINN with soft constraint loss used in this study

Table 3 Input variables for the HD-PINN

Category	Input variables	Symbol
Collocation points	Number of spatial collocation points[1]	N_x
	Number of temporal collocation points[1]	N_t
Boundary conditions	Left pressure boundary	p_l
	Right pressure boundary	p_r
	Left cavitation boundary[2]	θ_l
	Right cavitation boundary[2]	θ_r
Lubricant properties	Relative velocity	v_{rel}
	Density	ρ
	Viscosity	η
Surface characteristics	Mean square roughness	R_q
	Shear flow factor	Φ^{τ}
	Pressure flow factor	Φ^{p}
Geometry and dynamics	Height vector	$[h_1, h_2, h_3, x_b]$
	Vertical velocity of the Seal	v_h
	Lubricant height	$h_{\text{lubricant}}$

[1] The HD-PINN receives the number of collocation points in space and time as input. Based on this input, it generates two uniformly distributed arrays: one for the spatial coordinates, x, and one for the temporal coordinates, t

[2] The HD-PINN requires only one of the two boundary conditions for cavitation to model cavitation phenomena. The second boundary condition is inherently determined by the lubricant film thickness and is therefore automatically accounted for. Consequently, only 17 input parameters are required

The training process employs five distinct loss functions. The residual loss function computes the extended Reynolds equation and requires ICs over the entire training domain, in addition to BCs for pressure and cavitation. Furthermore, specific boundary and ICs are implemented as separate loss functions to ensure compliance. Another loss function, based on the Fischer-Burmeister equation, models the relationship between the pressure and the cavitation. However, this approach is insufficient for accurately predicting transition regions where the approach to zero of the cavitation is accompanied by a tendency towards non-zero values of pressure. To address this challenge, an additional loss function that employs soft constraints is introduced. This method, initially proposed by Rom [36], is designed to overcome the limitations of the Fischer-Burmeister equation in transition regions.

Given the considerable variability in the magnitudes of the different loss functions, it is crucial to apply appropriate weightings. To achieve this, a loss balancing algorithm is

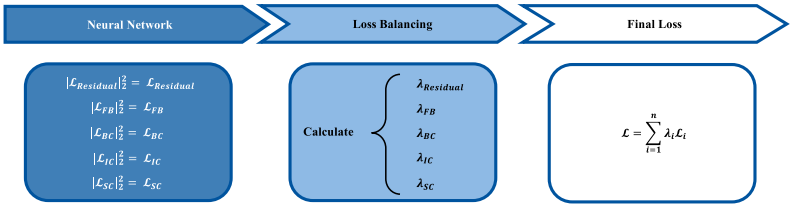

Fig. 3 Loss balancing

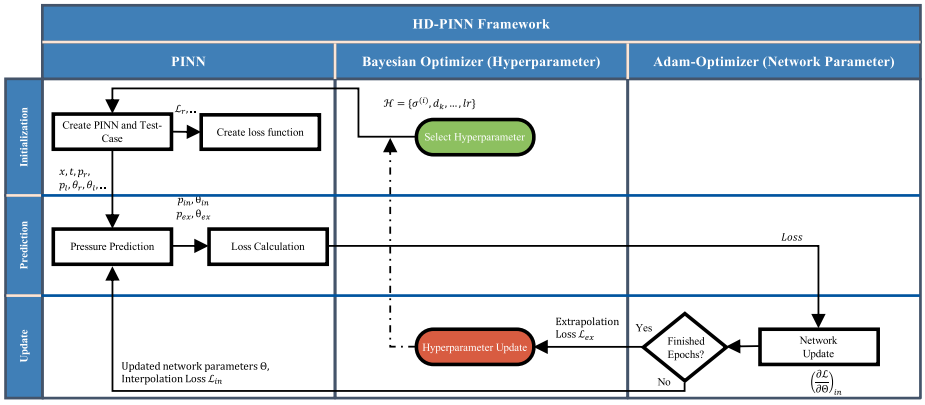

Fig. 4 HD-PINN Framework

implemented, which is based on earlier work by Bischof et al. [76], see Fig. 3. Subsequently, the total loss is determined by a weighted summation of the individual loss functions, which are then subjected to an Adam optimizer.

Training procedure

An overview of the HD-PINN framework is presented in Fig. 4. In order to identify appropriate hyperparameters ($\mathcal{H}$) that will enhance extrapolation capability, Bayesian optimization is employed. This probabilistic method of identifying a coherent set of parameters from a set of unknown parameters provides a starting point for further optimization. Multiple training trials run in an outer loop until promising hyperparameters are found. For each training, a PINN and the corresponding loss functions are initialized.

Here, additional loss functions are defined to evaluate the pressure p_{ex} and cavitation θ_{ex} outside the training area. These are structured in the same way as the loss functions that have already been presented. The only difference is that the collocation points used to calculate the pressure and cavitation are located outside the training domain, i.e. in the extrapolation domain. For the case, that the collocation points are set inside the training domain the extrapolation loss becomes the classical interpolation loss. In a manner analogous to the original loss calculation, these loss functions contain the partial derivatives, which, however, originate from the extrapolation range. The boundary and ICs are determined by the previously defined test range. These modifications are employed to compute the extrapolation loss, wherein the weighting coefficients remain unaltered. The sum of the extrapolation loss is conveyed to the Bayesian optimizer subsequent to each training trial, which searches for the optimal hyperparameter configuration with the lowest extrapolation loss. Notably, the extrapolation loss is not included in the actual training but is solely utilized to optimize the hyperparameters.

Table 4 summarizes the hyperparameters within the HD-PINN framework explored in this study and their respective value ranges. The initial hyperparameter ranges were based on the suggested values by Bischof et al. [76] and were further refined through previous research on PINNs addressing sealing movement and transient cavitation [22,23].

For the actual PINN training, the five losses are calculated with the help of the evaluated pressure p_{in} and cavitation θ_{in} inside the training domain. Adam optimizer then updates all neurons. After finding promising hyperparameters, these can be further finetuned manually or a longer training session can be started to train a final PINN.

Results

This section presents the results of the HD-PINN for the extrapolation tasks of the two test cases. The following subsections contain the predictions of the PINNs, which were trained on different spatial and temporal domains. In both cases, the training domain is successively reduced while the extrapolation domain is increased. The predictions of all PINNs are presented across the entire spatial testing domain alongside the validation data from the DDS for different time steps.

Sealing movement

In the first test case, both the spatial and temporal dimensions are successively reduced in steps of 0.25. This results in the training domain being divided into nine distinct combinations, with $x_{Train} \in \{0.75, 0.5, 0.25\}$ and $T_{Train} \in \{0.75, 0.5, 0.25\}$. The predictions of all PINNs are presented across the entire spatial testing domain alongside the validation data from the ifas DDS for the different time steps $t \in \{0, 0.25, 0.5, 0.75, 1\}$. Table 5 shows the hyperparameter and Figs. 5, 6, 7 illustrate the predictions of the PINNs trained on the spatial interval $x = [0, x_{Train}]$, where $x_{Train} = 0.75$ and T_{Train} varies. A comparison of the predicted pressure distributions for the individual networks reveals that they make distinct predictions. At initial time $t = 0$, all models are within the temporal interpolation range. It can be observed that they make highly accurate predictions in the spatial interpolation range. Furthermore, they also provide accurate predictions outside the interpolation range, up to a certain distance from the boundary of the convex hull of the interpolation range. The same can be observed for $t = 0.25$. Here, the predictions of all three models are also within the temporal interpolation range. Thes yield congruent results both within the interpolation range and up to a certain distance from their boundary. From time $t = 0.5$, only the PINN with $T_{Train} = 0.25$ is in the temporal extrapolation range. Notwithstanding the temporal extrapolation, it is evident that the predictions of this model are congruent with those of the other PINNs. At the time $t = 0.75$, two PINNs with $T_{Train} = 0.25$ and $T_{Train} = 0.5$ are present in the temporal extrapolation range. For the first time, a minor discrepancy in the spatial interpolation range emerges for the network with $T_{Train} = 0.25$. At time $t = 1$, all PINNs are within the temporal extrapolation range. The deviation for the network with $T_{Train} = 0.25$ is particularly evident, while the predictions of the other PINNs in the spatial interpolation range and in the vicinity of their convex hull are congruent with the results of the ifas DDS.

Table 6 shows the hyperparameter for the PINNs trained on the spatial interval $x = [0, x_{Train}]$, where $x_{Train} = 0.5$. The following figures, referenced as Figs. 8, 9, 10, demonstrate the predictions of the PINNs.

Table 4 Hyperparameter configuration range for both test scenarios

Category	Hyperparameter	Value range
Network architecture	Number of hidden layers d_k	[2, 8]
	Number of neurons per Layer $m^{(i)}$	[2, 256]
	Activation functions $\sigma^{(i)}$	{tanh, sigmoid, gelu, elu, softplus, swish}
Training process (Adam optimizer)	Number of Epochs E	$[10^4, 1.2 \cdot 10^5]$
	Learning rate lr	$[10^{-6}, 10^{-2}]$
Adaptive loss balancing (ReLoBRaLo)	Exponential decay rate α	[0, 1]
	Temperature $\mathcal{T}$	$[10^{-6}, 10^{2}]$
	Expected Saudade $\mathbb{E}(\rho)$	[0, 1]
Soft constraints[1]	Pressure threshold p_{thresh}	{0.005}
	Cavitation threshold θ_{thresh}	{0.1}
	Threshold for cavitation change $\left(\frac{\partial \theta}{\partial x}\right)_{thresh}$	{15}
	Number of adaption points $n_{cp_{added}}$	{15}

[1]The settings for soft constraints are only relevant for the modelling of cavitation phenomena

Table 5 Bayesian-optimized hyperparameter configurations for HD-PINNs trained on the sealing movement test case, with spatial bound $x_{\text{Train}} = 0.75$

HP	$T_{Train} = 0.75$	$T_{Train} = 0.5$	$T_{Train} = 0.25$
d_k	6	4	5
$m^{(i)}$	(128, 64, 64, 64, 64, 32)	(128, 64, 128, 64)	(32, 32, 64, 128, 64)
$\sigma^{(i)}$	(sigmoid, sigmoid, elu, gelu, swish, gelu)	(swish, tanh, tanh, softplus)	(tanh, gelu, tanh, swish, gelu)
E	19987	19824	19878
lr	$7.47 \cdot 10^{-5}$	$1.5046 \cdot 10^{-4}$	$2.3 \cdot 10^{-4}$
α	0.4007	0.6568	0.7839
$\mathcal{T}$	0.00047	0.00293	$2.25 \cdot 10^{-6}$
$\mathbb{E}(\rho)$	0.2619	0.2109	0.5971

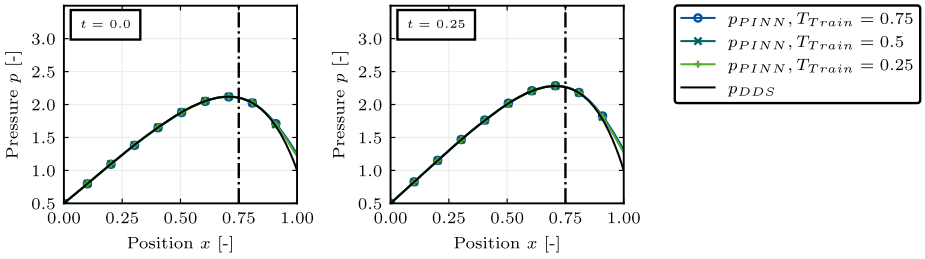

Fig. 5 Sealing Movement Test Case with HD-PINNs trained on the spatial domain [0, 0.75] and different temporal domains [0, T_{Train}], shown for $t = 0.0$ (left) and $t = 0.25$ (right)

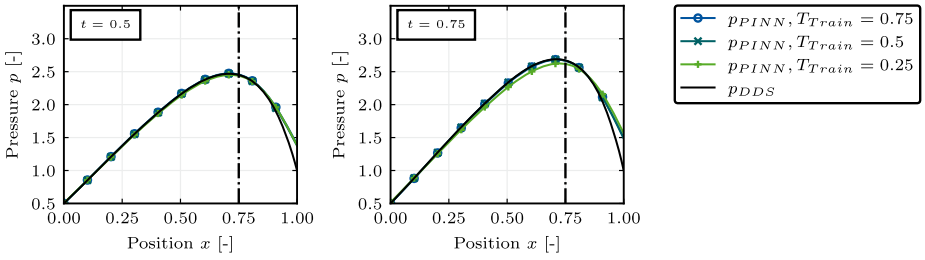

Fig. 6 Sealing Movement Test Case with HD-PINNs trained on the spatial domain [0, 0.75] and different temporal domains [0, T_{Train}], shown for $t = 0.5$ (left) and $t = 0.75$ (right)

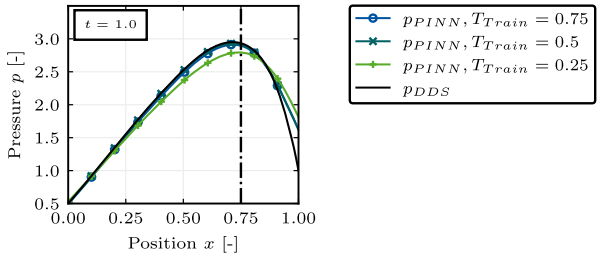

Fig. 7 Sealing Movement Test Case with HD-PINNs trained on the spatial domain [0, 0.75] and different temporal domains [0, T_{Train}], shown for $t = 1$

As previously stated, T_{Train} varies. Within the temporal interpolation range, the pressure distributions of the models show extensive agreement with the outputs of the ifas DDS in the spatial interpolation range. In contrast to the previous results for $x_{Train} = 0.75$, it can be observed that the predictions of the different models in the extrapolation range already diverge from the initial time point $t = 0$. Notwithstanding the fact that this range was taken into account during the training process of the three models, the predictions produced

Table 6 Bayesian-optimized hyperparameter configurations for HD-PINNs trained on the sealing movement test case, with spatial bound $x_{\text{Train}} = 0.5$

HP	$T_{Train} = 0.75$	$T_{Train} = 0.5$	$T_{Train} = 0.25$
d_k	3	5	5
$m^{(i)}$	(64, 128, 64)	(64, 64, 128, 64, 128)	(128, 128, 32, 128, 32)
$\sigma^{(i)}$	(gelu, gelu, softplus)	(tanh, swish, gelu, tanh, softplus)	(elu, tanh, elu, elu, sigmoid)
E	19995	19944	17307
lr	$4.4343 \cdot 10^{-5}$	$1.1940 \cdot 10^{-4}$	0.001
α	0.0255	0.2899	0.5236
$\mathcal{T}$	1.2307	5.1780	$9.7700 \cdot 10^{-4}$
$\mathbb{E}(\rho)$	0.7335	0.8088	0.5931

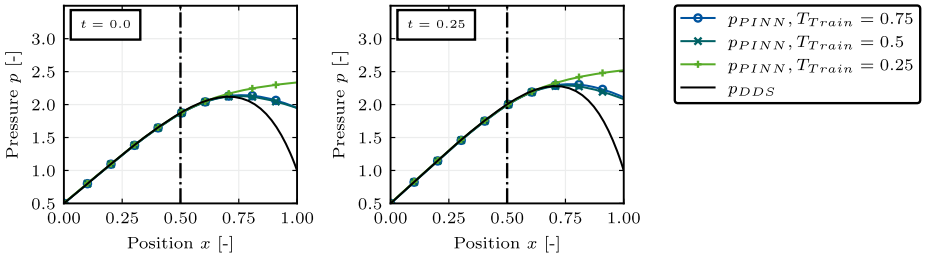

Fig. 8 Sealing Movement Test Case with HD-PINNs trained on the spatial domain [0, 0.5] and different temporal domains [0, T_{Train}], shown for $t = 0.0$ (left) and $t = 0.25$ (right)

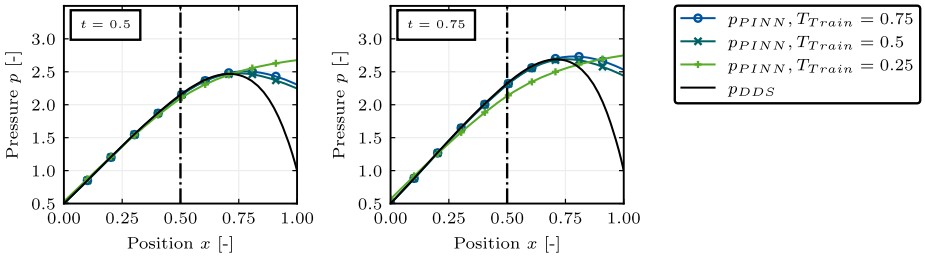

Fig. 9 Sealing Movement Test Case with HD-PINNs trained on the spatial domain [0, 0.5] and different temporal domains [0, T_{Train}], shown for $t = 0.5$ (left) and $t = 0.75$ (right)

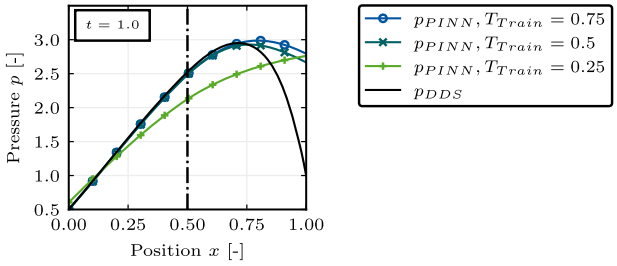

Fig. 10 Sealing Movement Test Case with HD-PINNs trained on the spatial domain [0, 0.5] and different temporal domains [0, T_{Train}], shown for $t = 1$

outside the training range exhibit notable discrepancies. The output pressure distribution of the PINN with $T_{Train} = 0.25$ exhibits the greatest discrepancy. The predicted pressure distributions of all PINNs align closely with the DDS up to a spatial interpolation limit of $t = 0.5$. However, a minor discrepancy between the DDS pressure distribution and the model prediction with $T_{Train} = 0.25$ can be observed. While the pressure distributions

Table 7 Bayesian-optimized hyperparameter configurations for HD-PINNs trained on the sealing movement test case, with spatial bound $x_{\text{Train}} = 0.25$

HP	$T_{Train} = 0.75$	$T_{Train} = 0.5$	$T_{Train} = 0.25$
d_k	3	2	4
$m^{(i)}$	(64, 32, 64)	(32, 32)	(32, 32, 32, 32)
$\sigma^{(i)}$	(softplus, gelu, sigmoid)	(gelu, sigmoid)	(gelu, elu, tanh, sigmoid)
E	19995	79985	53084
lr	$1.9942 \cdot 10^{-5}$	$3.783 \cdot 10^{-4}$	$4.57 \cdot 10^{-4}$
α	0.3766	0.8902	0.9273
$\mathcal{T}$	$1.4919 \cdot 10^{-3}$	$3.429 \cdot 10^{-5}$	$2.489 \cdot 10^{-6}$
$\mathbb{E}(\rho)$	0.6610	0.0322	0.0430

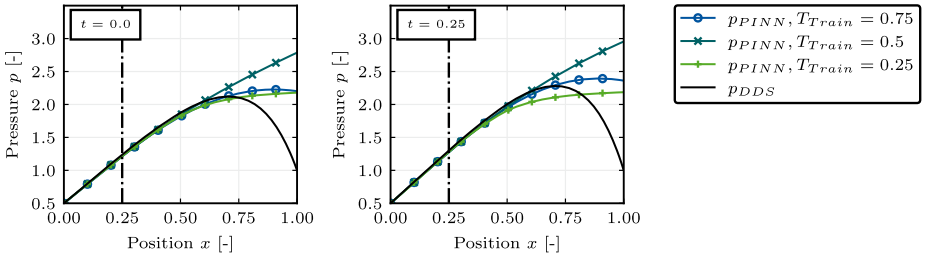

Fig. 11 Sealing Movement Test Case with HD-PINNs trained on the spatial domain [0, 0.25] and different temporal domains [0, T_{Train}], shown for $t = 0$ (left) and $t = 0.25$ (right)

for $T_{Train} = 0.5$ and $T_{Train} = 0.75$ remain relatively close to the calculations of the DDS until the end of the test time frame, it can be observed that the inaccuracies of the PINN's predictions for $T_{Train} = 0.25$ increase significantly with increasing temporal development.

Table 7 and Figs. 11, 12, 13 show the hyperparameter and predictions of those PINNs that have been trained on the spatial interval $x = [0, x_{Train}]$, where $x_{Train} = 0.25$ and the temporal domain boundary T_{Train} vary, respectively.

We also recognize here that the predictions of the PINNs within the interpolation range match the output of the DDS very accurately. At time $t = 0$, we also recognize here that the predictions of the three different models differ from each other outside the spatial area seen. Nevertheless, all models show a congruence with the DDS, up to $x \approx 0.5$. Only the predicted pressure distributions of the PINNs with $T_{Train} = 0.5$ and $T_{Train} = 0.75$ show a gradient in the right direction from this point onwards. The temporal development shows that the predictions in the extrapolation areas deviate more and more from the values of the ifas DDS. While the pressure distribution of the PINN with $T_{Train} = 0.75$ only gradually approaches a gradient drop in the x-direction, the model with $T_{Train} = 0.25$ exhibits a much earlier gradient drop. The PINN with $T_{Train} = 0.5$ demonstrates a consistently low gradient drop in the extrapolation range throughout the simulation. The right-hand BC of the test range fails to meet the standards set by this PINN. The results presented in this subsection demonstrate that the pressure distribution of the PINNs is consistently congruent with the output of the DDS in the interpolation range. As the distance from the interpolation range's convex hull increases, the PINNs' predictions exhibit a greater and greater degree of deviation in the extrapolation.

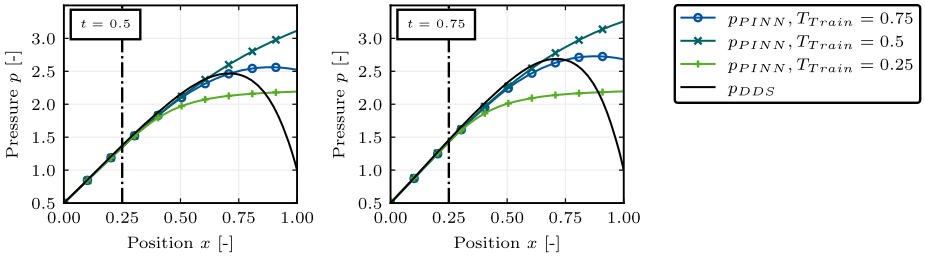

Fig. 12 Sealing Movement Test Case with HD-PINNs trained on the spatial domain [0, 0.25] and different temporal domains [0, T_{Train}], shown for $t = 0.5$ (left) and $t = 0.75$ (right)

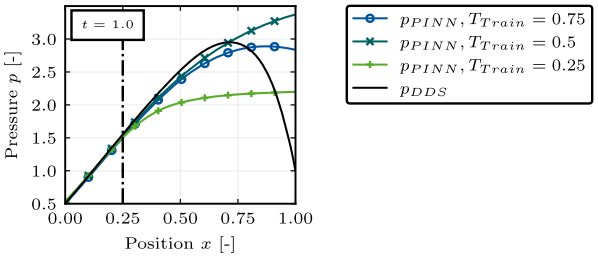

Fig. 13 Sealing Movement Test Case with HD-PINNs trained on the spatial domain [0, 0.25] and different temporal domains [0, T_{Train}], shown for $t = 1$

Table 8 Bayesian-optimized hyperparameter configuration for HD-PINNs trained on the transient cavitation test case

HP	$T_{Train} = 1.0$
d_k	7
$m^{(i)}$	(32, 32, 32, 32, 32, 32, 32)
$\sigma^{(i)}$	(gelu, elu, swish, softplus, gelu, gelu, sigmoid)
E	120000
lr	$3.246 \cdot 10^{-4}$
α	0.9805
$\mathcal{T}$	$1.609 \cdot 10^{-6}$
$\mathbb{E}(\rho)$	0.0322
p_{thresh}	0.005
θ_{thresh}	0.1
$\left(\frac{\partial \theta}{\partial x}\right)_{thresh}$	15
$n_{cp_{added}}$	15

Transient cavitation

In the second test case, the temporal dimensions are successively reduced in steps of 0.2. This results in the temporal training domain partitioning into four different variations, with $T_{Train} \in \{0.8, 0.6, 0.4, 0.2\}$. The predictions of all the PINNs are presented, showing the pressure and cavitation distribution over the entire spatial test domain. These predictions are compared to the validation data from the DDS for different time steps $t \in \{0, 0.2, 0.4, 0.6, 0.8, 1\}$. Table 8 illustrates the set of hyperparameters used for the investigated PINNs obtained from a previously published paper regarding the solution of a transient cavitation test case [22].

Figure 14 illustrates the pressure and cavitation distribution at times $t = 0$ and $t = 0.2$ for a model that was trained up to $T_{\text{Train}} = 0.8$. The initial state at $t = 0$ is predicted by the network to be congruent with the DDS output. At $t = 0.2$, the model is in the

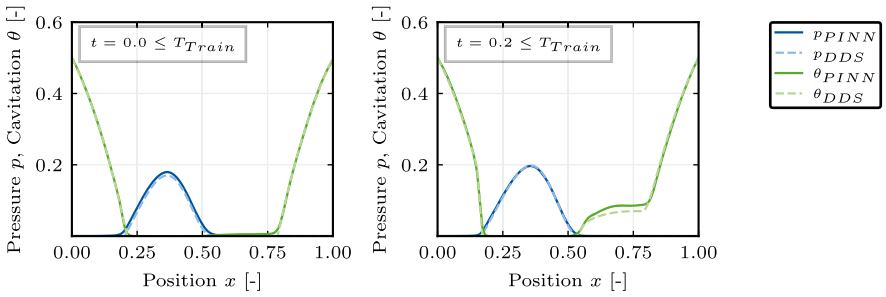

Fig. 14 Pressure and cavitation distribution at $t = 0$ (left) and $t = 0.2$ (right) for the transient cavitation test case, with HD-PINN trained on the temporal domain [0, 0.8]

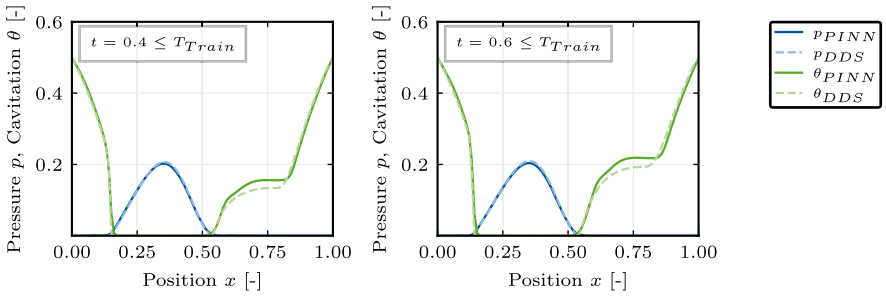

Fig. 15 Pressure and cavitation distribution at $t = 0.4$ (left) and $t = 0.6$ (right) for the transient cavitation test case, with HD-PINN trained on the temporal domain [0, 0.8]

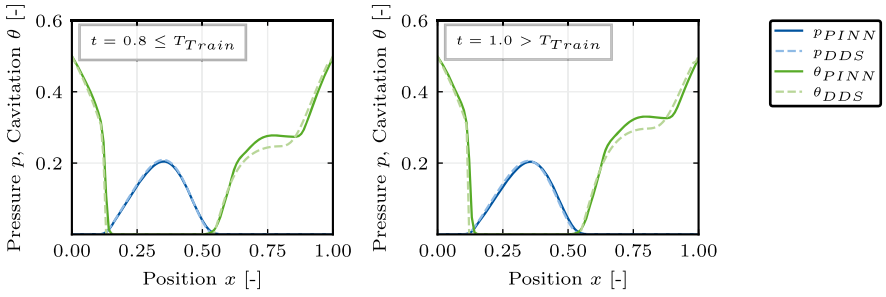

Fig. 16 Pressure and cavitation distribution at $t = 0.8$ (left) and $t = 1$ (right) for the transient cavitation test case, with HD-PINN trained on the temporal domain [0, 0.8]

interpolation range and also delivers largely congruent results. The only instance where the cavitation distribution deviates from that of the DDS is in the range $x \in [0.55, 0.80]$.

Figure 15 shows the prediction of the pressure and cavitation distribution at times $t = 0.4$ and $t = 0.6$. Here, the pressure distribution is shown to be congruent, whereas in the same spatial range $x \in [0.55, 0.80]$ the deviation remains.

Figure 16 depicts the prediction for the time points $t = 0.8$ and $t = 1$. The latter represents the first temporal extrapolation of the PINN. While the deviation of the cavitation distribution behind the pressure peak remains the same, the pressure distribution of the model is still an accurate approximation of the DDS.

The following figures illustrate the temporal development of the pressure and cavitation distribution of a PINN trained up to $T_{\text{Train}} = 0.6$. Figure 17 shows a deviation in the pressure distribution at $t = 0$, which aligns with the pressure distribution of the ifas DDS at $t = 0.2$.

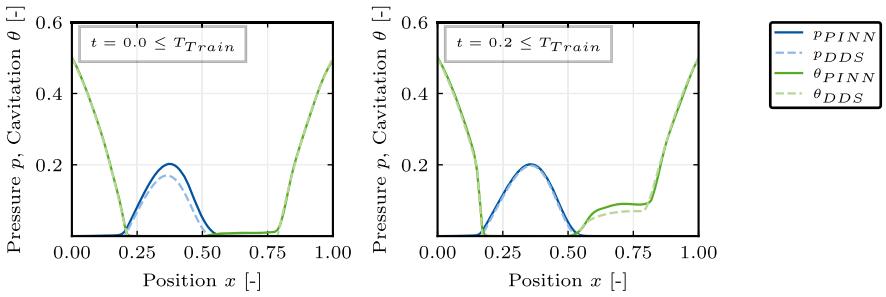

Fig. 17 Pressure and cavitation distribution at $t = 0$ (left) and $t = 0.2$ (right) for the transient cavitation test case, with HD-PINN trained on the temporal domain [0, 0.6]

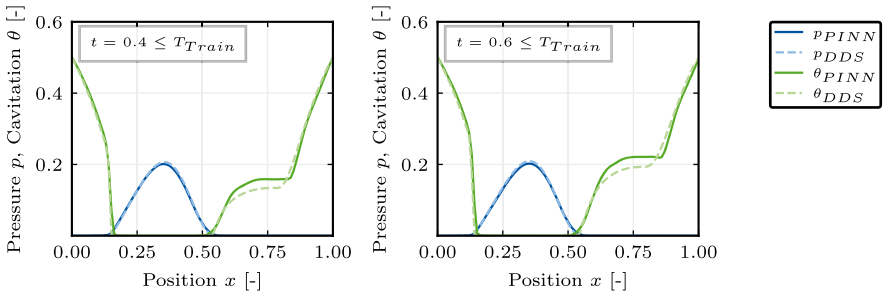

Fig. 18 Pressure and cavitation distribution at $t = 0.4$ (left) and $t = 0.6$ (right) for the transient cavitation test case, with HD-PINN trained on the temporal domain [0, 0.6]

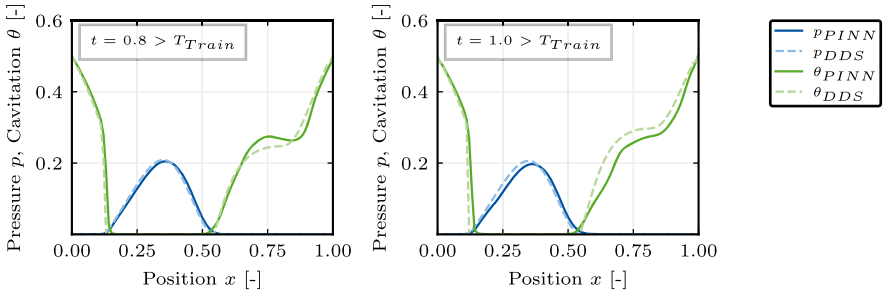

Fig. 19 Pressure and cavitation distribution at $t = 0.8$ (left) and $t = 1$ (right) for the transient cavitation test case, with HD-PINN trained on the temporal domain [0, 0.6]

In Fig. 18, it can be seen that the cavitation distribution in the regions behind the pressure area exhibits a smaller deviation compared to the PINN trained up to $T_{\text{Train}} = 0.8$.

Figure 19, demonstrates the model's behaviour in extrapolation tasks. The predictions at $t = 0.8$ are largely congruent. At $t = 1$, a difference between the model prediction and the ifas DDS is noticeable. Nevertheless, the direction of the gradients in the cavitation distribution is consistent with that of the ifas DDS.

Subsequently, the temporal training range is further reduced to $T_{\text{Train}} = 0.4$. Figure 20 shows the pressure and cavitation distribution for such a PINN. The results obtained show a high level of agreement with the validated simulations. The predictions shown in Fig. 21 also show almost complete agreement with the ground truth outputs. It should be noted that the PINN was extrapolated at time $t = 0.6$ and still makes such accurate predictions. The predictions shown in Fig. 22 approximate the pressure and cavitation distribution of the validated simulation. A small deviation is recognizable. However, it should be noted

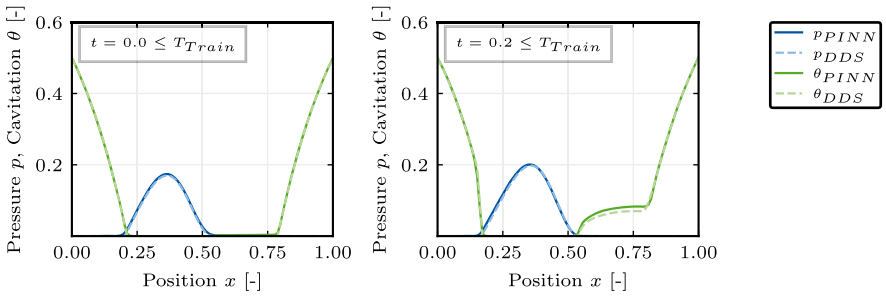

Fig. 20 Pressure and cavitation distribution at $t = 0$ (left) and $t = 0.2$ (right) for the transient cavitation test case, with HD-PINN trained on the temporal domain [0, 0.4]

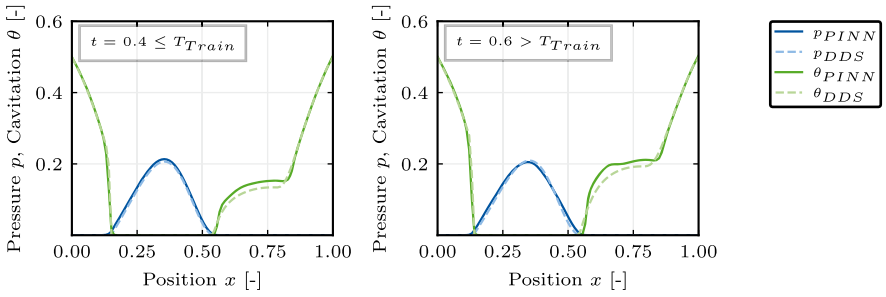

Fig. 21 Pressure and cavitation distribution at $t = 0.4$ (left) and $t = 0.6$ (right) for the transient cavitation test case, with HD-PINN trained on the temporal domain [0, 0.4]

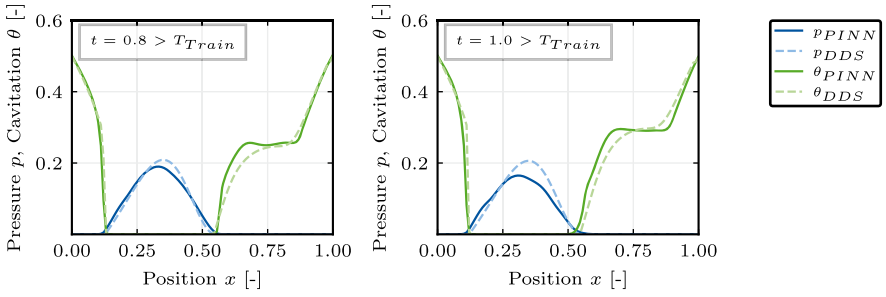

Fig. 22 Pressure and cavitation distribution at $t = 0.8$ (left) and $t = 1$ (right) for the transient cavitation test case, with HD-PINN trained on the temporal domain [0, 0.4]

that the gradients of the predicted pressure and cavitation distribution have a similar direction to those of the ifas DDS. Finally, the results are shown for the PINN that was only trained up to $T_{\text{Train}} = 0.2$. In Fig. 23, it can be observed, especially at $t = 0.2$, that the PINN gives more accurate predictions in the previously mentioned range of $x \in [0.55, 0.8]$. Figure 24 shows this PINN for the first time in extrapolation tasks. It quickly becomes clear that the prediction of the pressure and cavitation distribution differs significantly from the ifas DDS distribution. In Fig. 25, the PINN predictions of pressure and cavitation are pushed towards zero, which does not correspond to the output of the ifas DDS.

Discussion

The potential of PINNs for hydrodynamic lubrication calculations is demonstrated by their use in extrapolation tasks. An additional significant advantage of PINNs is demon-

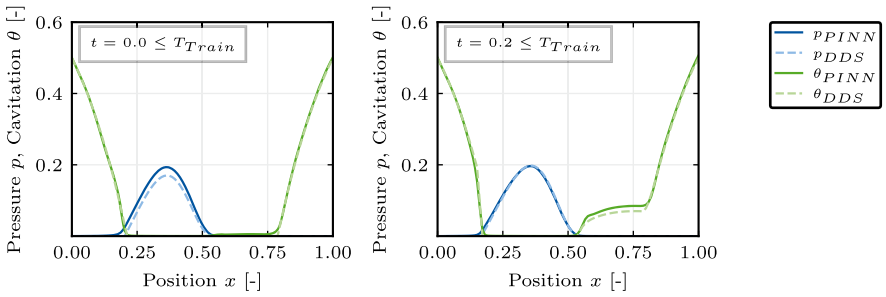

Fig. 23 Pressure and cavitation distribution at $t = 0$ (left) and $t = 0.2$ (right) for the transient cavitation test case, with HD-PINN trained on the temporal domain [0, 0.2]

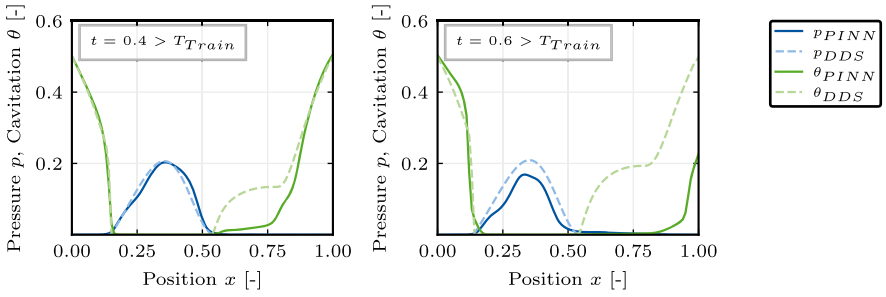

Fig. 24 Pressure and cavitation distribution at $t = 0.4$ (left) and $t = 0.6$ (right) for the transient cavitation test case, with HD-PINN trained on the temporal domain [0, 0.2]

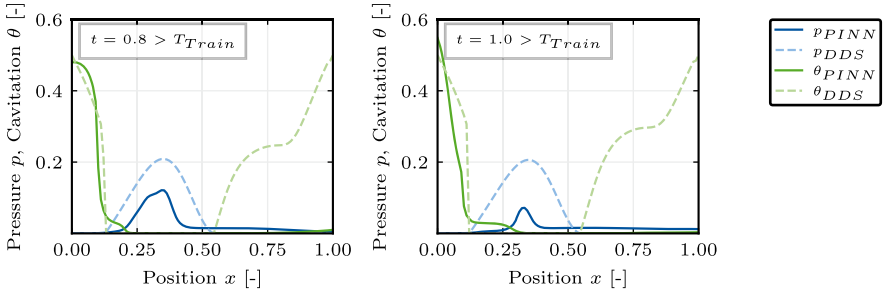

Fig. 25 Pressure and cavitation distribution at $t = 0.8$ (left) and $t = 1$ (right) for the transient cavitation test case, with HD-PINN trained on the temporal domain [0, 0.2]

Table 9 Comparison of prediction speed between HD-PINN model and a rigid DDS

Method[1]	Average prediction time (ms)	Speed factor
rigid DDS	1200	–
HD-PINN	6 ± 2	$150 - 300\times$

[1]The results were obtained on a PC running Windows 10 with an Intel(R) Xeon(R) CPU E5-1680 v3 @ 3.2 GHz (16 CPUs)

strated in Table 9. For the simulations conducted, the factor was $150 - 300$ in the computing time between HD-PINN and the traditional counterpart of the rigid ifas DDS.

A current limitation of the HD-PINN is the neglect of time dependencies in the NN itself. This poses a challenge in temporal extrapolation, especially for the cavitation regime, since cavitation exhibits a time dependence term in the Reynolds equation, which can be observed in the cavitation regime after the pressure peak in Figs. 24 and 25. This observation is supported by the more accurate prediction of cavitation before the pressure peak, as it does not vary to the same extent as in the post-peak regime. To solve this issue

and improve the generalizability, instead of Fully Connected Networks (FCNs), Recurrent Neural Networks (RNNs) or Long Short-Term Memory Networks (LSTMs) can achieve better extrapolation capability. The application of physics-informed losses in RNNs [77] and LSTMs [78] has already been successfully implemented and investigated for extrapolation tasks [79,80]. Another notable method is the so-called PINNsFormer, an architecture that uses attention mechanisms to capture deeper correlations [81]. Compared to temporal extrapolation, spatial extrapolation is more prone to errors, especially compared to the observed accuracy in the interpolation regime. These results also match prior research on spatial extrapolation for hydrodynamic lubrication for a more simplified variant of the Reynolds equation and gap geometry [20]. The PINN requires an understanding of the investigated geometry. However, four height parameter inputs aim to represent the whole geometry. To tackle this issue, Rom extended his PINN's input, which was applied to journal bearings by the relative eccentricity [36]. In the case of a sealing gap, a single additional physical parameter can not be defined for all several geometries; therefore, implementing a geometry-aware PINN (GA-PINN) framework [82] could improve this issue. In this case, custom input parameters do not describe the geometry. Instead, the gap geometry is sampled and passed to an autoencoder, which reduces the high-dimensional input to a low-dimensional latent space and then passes to the PINN with the spatial and time coordinates. A noteable type of network is the Convolutional Neural Network (CNN), which is frequently used for processing of high-dimensional input, like images and can be integrated in the autoencoder. The combination of a physics-informed loss and a CNN has already been successfully investigated for space-time problems [83]. Another promising approach is graph neural networks (GNNs) [84,85], which aim to process the input represented in the graph domain directly and have already been implemented in a physics-informed GNN (PI-GNN) [86]. The HD-PINN has many hyperparameters, mainly due to the sophisticated loss balancing. Using the model-based Bayesian optimizer automates the process of finding suitable hyperparameters. For each PINN solving the sealing movement test scenario, a set of suitable hyperparameters has been obtained and listed in Tables 5, 6 and 7. For the transient cavitation test case, where the spatial domain was kept constant, and the temporal domain was reduced, a hyperparameter set was used, which is shown in Table 8. As the Bayesian optimizer can select continuously within the range of hyperparameters provided, it is doubtful that the exact same set of hyperparameters will be obtained for different test cases. However, there is no clear trend in the hyperparameters for changing the spatial and temporal training domain. For example, the decay rate α increases for decreasing temporal training domain and constant spatial training domain but increases and decreases for decreasing x_{Train} and constant T_{Train}. The temperature does not show a clear trend for changing spatial or temporal training domains. Due to the high dimensionality created by the available number of hyperparameters, several sets might exhibit suitable performance but may not show a trend toward changing scenarios. For a deeper understanding of the influence of the hyperparameters, a further study is required, firstly to obtain a set of hyperparameters for each PINN solving the transient cavitation, and secondly to investigate whether different sets of hyperparameters could lead to the same performance in terms of interpolation and extrapolation of a test case.

To sum up, the results of this study are highly significant. The ability of PINNs to extrapolate both spatially and temporally was demonstrated using two hydrodynamic test cases. For both test cases, the HD-PINN already has a very accurate prediction capability

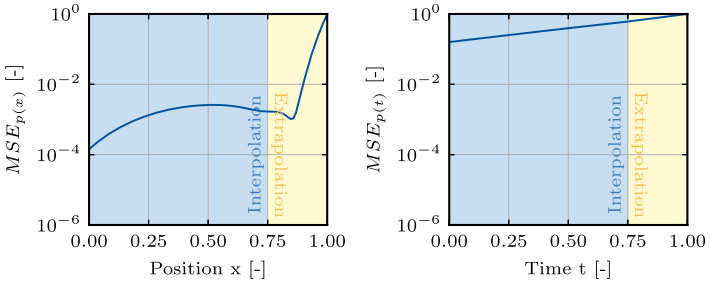

Fig. 26 Normalized MSE between the predictions of the PINN, with $x_{Train} = 0.75$ and $T_{Train} = 0.75$, and the reference values of the rigid DDS data in both spatial and temporal domains. The MSE is normalized with respect to the maximum error value: 0.18884 (left) and 0.012587 (right)

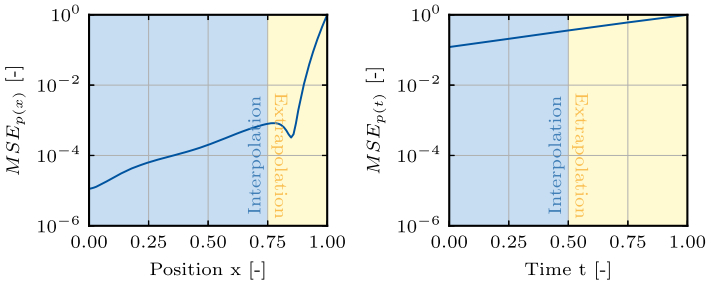

Fig. 27 Normalized MSE between the predictions of the PINN, with $x_{Train} = 0.75$ and $T_{Train} = 0.5$, and the reference values of the rigid DDS data in both spatial and temporal domains. The MSE is normalized with respect to the maximum error value: 0.17914 (left) and 0.011865 (right)

in the interpolation domain. This was also demonstrated in the extrapolation domain, which was sufficiently close to the convex hull of the interpolation domain. This section is devoted to the discussion. The normalized mean squared error (MSE) between the rigid ifas DDS and the differently trained PINNs in the respective test cases is used to highlight and discuss the differences between the predictions in the interpolation and extrapolation domains. Therefore a quantitative analysis, besides the qualitative analysis is provided.

Sealing movement

This subsection presents an analysis of the behavior of the PINNs in the context of spatial and temporal interpolation and extrapolation. The metric employed for this analysis is the mean squared error (MSE), which has been normalized to the maximum error between the rigid ifas DDS and the PINNs. The following figures illustrate the normalized MSE in the spatial and temporal directions for PINNs with $x_{\text{Train}} \in \{0.75, 0.5, 0.25\}$ and $T_{\text{Train}} \in \{0.75, 0.5, 0.25\}$. It can be observed that the discrepancy between the PINNs and the rigid ifas DDS increases significantly in the x-direction beyond the spatial interpolation limit. Similarly, the discrepancy in the temporal dimension also increases, though to a lesser extent than in the spatial dimension (Figs. 26, 27, 28).

Another discernible pattern can be identified. It can be demonstrated that as the spatial interpolation ranges become smaller, the $MSE_{p(t)}$ increases. This phenomenon can be observed in the right-hand plots. This indicates that the extrapolation capability is diminished as the training range is narrowed (Figs. 29, 30, 31, 32, 33, 34).

The kink in the $MSE_{p(x)}$ graph within the extrapolation region is attributed to the pressure gradient drop of the rigid ifas DDS in this region. In contrast, the PINN predicts

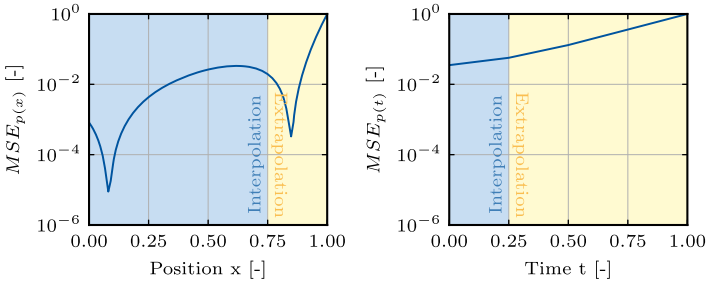

Fig. 28 Normalized MSE between the predictions of the PINN, with $x_{Train} = 0.75$ and $T_{Train} = 0.25$, and the reference values of the rigid DDS data in both spatial and temporal domains. The MSE is normalized with respect to the maximum error value: 0.24769 (left) and 0.03659 (right)

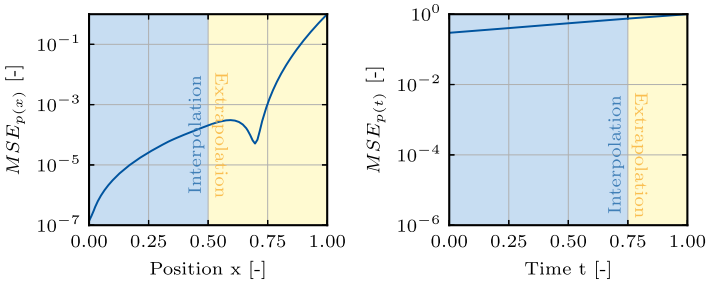

Fig. 29 Normalized MSE between the predictions of the PINN, with $x_{Train} = 0.5$ and $T_{Train} = 0.75$, and the reference values of the rigid DDS data in both spatial and temporal domains. The MSE is normalized with respect to the maximum error value: 1.87879 (left) and 0.16923 (right)

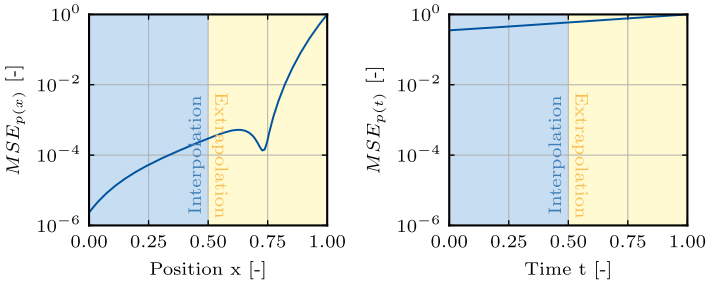

Fig. 30 Normalized MSE between the predictions of the PINN, with $x_{Train} = 0.5$ and $T_{Train} = 0.5$, and the reference values of the rigid DDS data in both spatial and temporal domains. The MSE is normalized with respect to the maximum error value: 1.69390 (left) and 0.13563 (right)

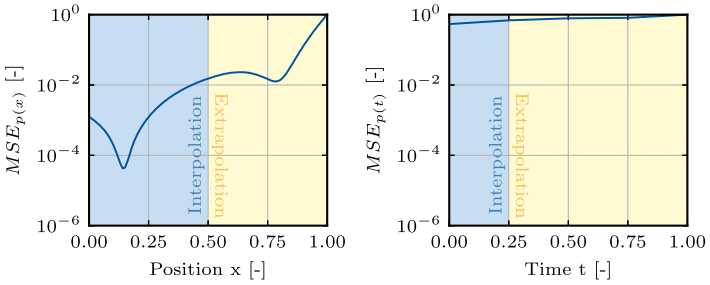

Fig. 31 Normalized MSE between the predictions of the PINN, with $x_{Train} = 0.5$ and $T_{Train} = 0.25$, and the reference values of the rigid DDS data in both spatial and temporal domains. The MSE is normalized with respect to the maximum error value: 2.61361 (left) and 0.20934 (right)

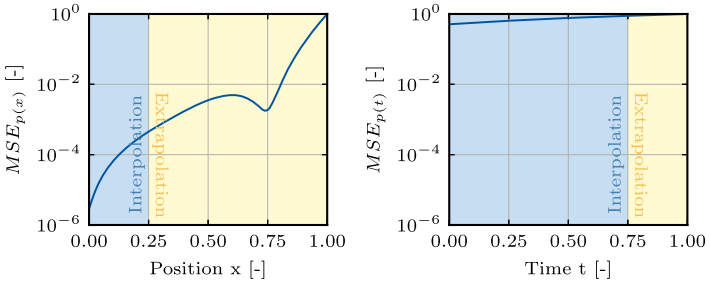

Fig. 32 Normalized MSE between the predictions of the PINN, with $x_{Train} = 0.25$ and $T_{Train} = 0.75$, and the reference values of the rigid DDS data in both spatial and temporal domains. The MSE is normalized with respect to the maximum error value: 2.36247 (left) and 0.17607 (right)

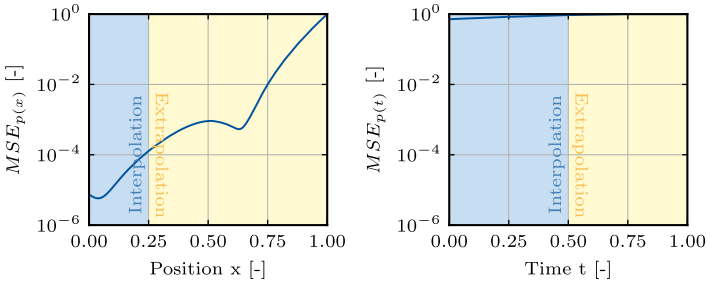

Fig. 33 Normalized MSE between the predictions of the PINN, with $x_{Train} = 0.25$ and $T_{Train} = 0.50$, and the reference values of the rigid DDS data in both spatial and temporal domains. The MSE is normalized with respect to the maximum error value: 4.44342 (left) and 0.33365 (right)

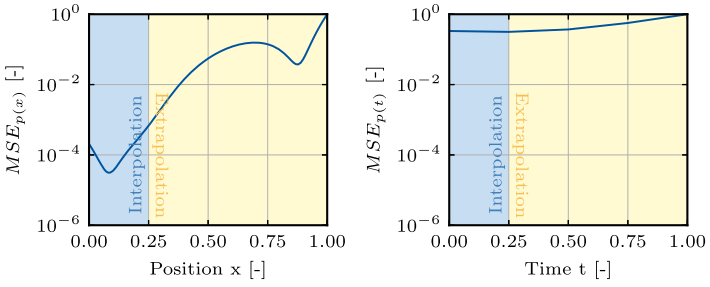

Fig. 34 Normalized MSE between the predictions of the PINN, with $x_{Train} = 0.25$ and $T_{Train} = 0.25$, and the reference values of the rigid ifas DDS data in both spatial and temporal domains. The MSE is normalized with respect to the maximum error value: 1.41619 (left) and 0.23464 (right)

a lower pressure gradient drop in this region, highlighting the struggle of the PINN to correctly predict the gradients in the extrapolation region. It has been shown that it is possible to extrapolate beyond both boundaries. The plots presented in this subsection confirm the findings from the literature regarding the extrapolation of PINNs: As the distance from the convex training envelope increases, the accuracy of the predictions deteriorates.

Transient cavitation

In order to discuss the results of the second case, it is necessary to consider the error metric MSE between the pressure and cavitation distributions predicted by the PINN with different T_{Train} and those output by the rigid DDS. This is shown for the pressure and cavitation predictions as a function of time t. Figure 35 shows that the mean square

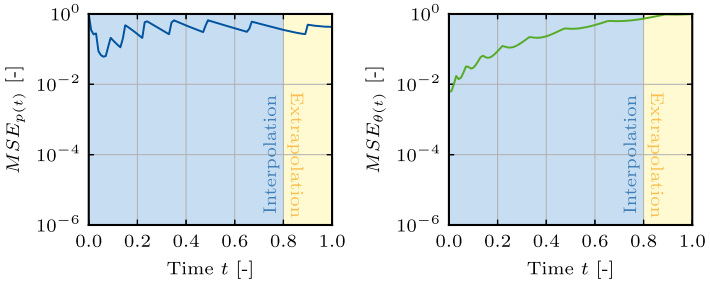

Fig. 35 Normalized MSE of PINNs' predictions relative to validated rigid ifas DDS data in the temporal domain. The MSE is normalized with respect to the maximum error value: 0.00004 (left) and 0.00155 (right)

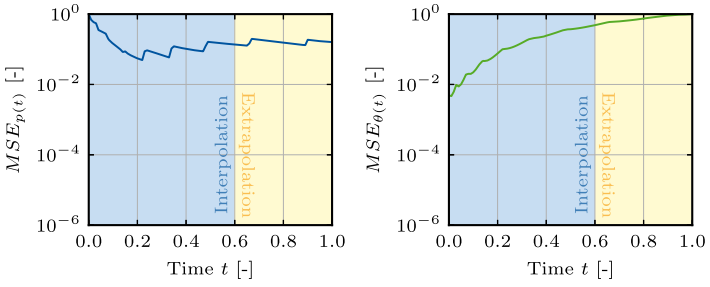

Fig. 36 Normalized MSE of PINNs' predictions relative to validated rigid DDS data in the temporal domain. The MSE is normalized with respect to the maximum error value: 0.00028 (left) and 0.00386 (right)

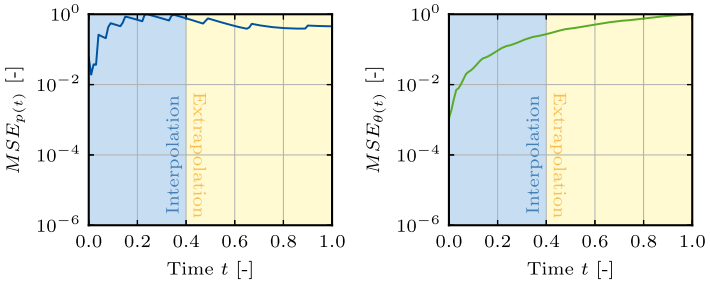

Fig. 37 Normalized MSE of PINNs' predictions relative to validated rigid DDS data in the temporal domain. The MSE is normalized with respect to the maximum error value: 0.00012 (left) and 0.00707 (right)

error increases in the temporal direction. However, it can be seen that it does not differ drastically in the temporal interpolation range from that in the extrapolation range for pressure distribution predictions. In contrast to the spatial extrapolation of the first test case, a pronounced exponential increase in the error in the temporal extrapolation is not observed. The MSE remains within a smaller size range with increasing time.

The same can be seen in Fig. 36 for the PINN with $T_{Train} = 0.6$. Here, the increased error at $t = 0$ is visible in the interpolation domain.

Between $T_{Train} = 0.6$ and $T_{Train} = 0.4$, there is no major difference in magnitude in the MSE for both the pressure and cavitation distributions, as can be compared with Fig. 37.

At $T_{Train} = 0.2$, the MSE increases significantly compared to the previous temporal training domains, as can be seen in Fig. 38. This test case also seems to confirm the theory that predictions become less reliable as the interpolation range becomes smaller. Nevertheless, the temporal extrapolation of the PINNs provides reliable predictions up to a certain distance from the training range.

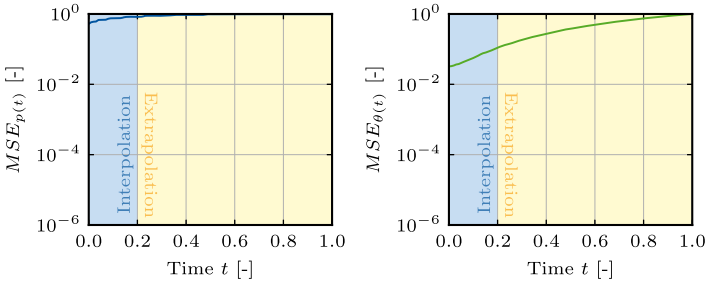

Fig. 38 Normalized MSE of PINNs' predictions relative to validated rigid DDS data in the temporal domain. The MSE is normalized with respect to the maximum error value: 0.00738 (left) and 0.01422 (right)

In this work, it has been shown that the temporal extrapolation of the pressure and cavitation distribution for a $T_{Train} = 0.4$ predicts reliably up to the time $t = 0.8$.

Conclusion and outlook

In particular, for real-world applications that require real-time simulation of complex tribological systems or applications that consist of several partial simulations and require fast internal computations, PINNs are highly suitable alternatives to conventional numerical methods. In particular, for seals, which are a key component of many engineering systems, especially in pneumatic valves, using PINNs to accelerate the solution of the EHL investigation is a promising innovation. The ability to gain a deeper understanding of the interplay between hydrodynamics, contact mechanics, and material properties in a reasonable amount of time enables an optimized seal's design and operation. EHL simulations such as the ifas DDS provide accurate solutions but have a significant drawback due to their iterative solution process, which requires extensive computing time. The presented HD-PINN represents a promising approach to develop an accelerated solution method for the ifas DDS, which has already been demonstrated in previous work for interpolation tasks [23]. Furthermore, PINNs are able to predict beyond their domain of definition. While PINNs are able to perform extrapolations as demonstrated in this work, traditional numerical methods are not. Consequently, the ICs and bounds must be reset for each new problem, and the process must be repeated until a solution is found. In contrast, PINNs are capable of adapting to new conditions and domains in a flexible manner, thereby delivering results. The results demonstrate that the extrapolation of the HD-PINN is of high quality in the immediate vicinity of the interpolation domain. However, the extrapolation quality declines, and the prediction error magnitude increases significantly outside this area. This finding was also seen in the studies by Kim et al., Fesser et al. and Bonfati et al. [73–75]. The spatial extrapolation is more susceptible to errors than the temporal extrapolation. This may be attributed to the fact that the HD-PINN does not accurately capture the spatial relationship with the height profile of the sealing gap. Another potential reason for the observed increase in error with increasing distance from the interpolation limit is that the PINN was trained on a specific case only and may not generalize to other physical relationships. To improve the generalizability for the spatial extrapolation a GA-PINN or PI-GNN could be integrated in the HD Framework. As the investigated PINNs were studied for two specific test cases, future research could investigate the extrapolation capability in a multi-case scenario that encompasses different geometries of the hydrodynamic lubrication gap, similar to prior conducted

research [20]. In addition, transfer learning approaches could be considered, whereby a pre-trained PINN contains fundamental knowledge and is further trained for specific use cases. This approach could significantly reduce the computational time required for training, as only a limited number of data sets would be necessary for ongoing training. Further research also includes investigating the hyperparameter. Firstly, the effect of the hyperparameter on the transient cavitation test scenario should be investigated by obtaining a set of hyperparameters for each extrapolation task with the Bayesian optimizer. Secondly, a deeper dive into the hyperparameters could lead to a better understanding of their effects on interpolation and extrapolation and overall PINN's performance. In the field of PIML, there are other promising approaches besides PINNs with great potential for extrapolation, especially in the field of temporal extrapolation. Instead of FCNs, RNNs or LSTMs or Transformers can be used to achieve improved extrapolation capability. In summary, PINNs are a promising and faster alternative to traditional PDE solvers and can, to some extent, provide reliable results outside the defined domain. However, there is still considerable potential to improve the extrapolation capability. Eventually, the HD-PINN will model the entire EHL simulation by extending it to include surface roughness, non-Newtonian fluid, and deformation. Recently, the framework successfully solved multi-case tasks with varying surface roughnesses [24]. The ifas DDS solves the EHL for a pneumatic valve; therefore, the lubricant is modeled as a non-Newtonian fluid and behaves according to Herschel-Bulkley (HB), which has already been modeled with PINNs [87]. Regarding the deformation, the DDS considers hyperelastic behavior; therefore, respective material models are integrated into the HD-PINN, similar to the approach of Nguyen et al., who solved hyperelastic deformation problems with PINNs [88].

Abbreviations

AD	Automatic differentiation
BC	Boundary conditions
CNN	Convolutional neural network
DDS	Dynamic description of sealings
EHL	Elastohydrodynamic lubrication
FEA	Finite element analysis
FCN	Fully connected networks
FEM	Finite element method
GA-PINN	Geometry-aware physics-informed neural network
GNN	Graph neural network
HB	Herschel-Bulkley
HD-PINN	Hydrodynamic-physics-informed neural network
IC	Initial conditions
ifas	Institute for fluid power drives and systems
JFO	Jakobsson-Floberg-Olsson
LSTM	Long short-term memory networks
MOR	Model order reduction
MSE	Mean squared error
NN	Neural network
HP	Hyperparameter
PDE	Partial differential equation
PI-GNN	Physics-informed graph neural network
PIML	Physics-informed machine learning
PINN	Physics-informed neural network
RNN	Recurrent Neural Networks
SS	Swift-Stieber
UEL	User-defined element

Acknowledgements
The authors thank the Research Association for Fluid Power of the German Engineering Federation VDMA for its financial support (Grant: FKM No. 7058400). Special gratitude is expressed to the participating companies and their representatives in the accompanying industrial committee for their advisory and technical support.

Author contributions
F. Brumand-Poor: Conceptualization, Methodology, Software, Validation, Formal Analysis, Investigation, Resources, Data Curation, Writing—Original Draft, Writing—Review & Editing, Visualization, Supervision, Project Administration, and Funding Acquisition. F.K. Azanledji: Conceptualization, Methodology, Software, Validation, Formal Analysis, Investigation, Data Curation, Writing—Original Draft, Writing—Review Editing, and Visualization. N. Plückhahn: Conceptualization, Software, and Writing—Review Editing. F. Barlog: Conceptualization, Software, and Writing—Review Editing. L. Boden: Software, Writing—Original Draft, and Writing—Review Editing. K. Schmitz: Conceptualization, Resources, Writing—Review Editing, Supervision, and Funding Acquisition.

Funding
Open Access funding enabled and organized by Projekt DEAL. This research paper is funded by Research Association for Fluid Power of the German Engineering Federation VDMA (Grant: FKM No. 7058400).

Availability of data and materials
The data that has been used is confidential.

Declarations

Ethics approval and consent to participate
Not applicable.

Consent for publication
Not applicable.

Competing interests
The authors declare that they have no competing interests.

Received: 2 September 2024 Accepted: 30 December 2024
Published online: 27 January 2025

References

1. Wohlers A, Heipl O, Persson BNJ, Scaraggi M, Murrenhoff H. Numerical and experimental investigation on o-ring-seals in dynamic applications. Int J Fluid Power. 2009;10:51–9.
2. Ping H. Numerical Calculation of Elastohydrodynamic Lubrication: Methods and Programs (Wiley, 2015). https://www.wiley.com/en-us/Numerical+Calculation+of+Elastohydrodynamic+Lubrication\%3A+Methods+and+Programs-p-9781118920992.
3. Dowson D, Higginson GR. A numerical solution to the elasto-hydrodynamic problem. J Mech Eng Sci. 1959;1:6–15.
4. Dakov N. Elastohydrodynamische simulation von wellendichtungen am beispiel der ptfe-manschettendichtung mit rückförderstrukturen.
5. Habchi W, Bair S, Vergne P. On friction regimes in quantitative elastohydrodynamics. Tribol Int. 2013;58:107–17.
6. Maier D. On the use of model order reduction techniques for the elastohydrodynamic contact problem.
7. Echávarri Otero J, de La Guerra Ochoa E, Chacón Tanarro E, Franco Martínez F, Contreras Urgiles RW. An analytical approach for predicting ehl friction: usefulness and limitations. Lubricants. 2022;10:141.
8. Simpson M, et al. An analytical friction model for point contacts subject to boundary and mixed elastohydrodynamic lubrication. Tribol Int. 2024;196: 109699.
9. Crook AW. The lubrication of rollers. Philos Trans Royal Soc Lond Ser A Math Phys Sci. 1958;250:387–409.
10. Gentle CR, Cameron A. Optical elastohydrodynamics at extreme pressures. Nature. 1973;246:478–9.
11. Sperka P, Krupka I, Hartl M. Analytical formula for the ratio of central to minimum film thickness in a circular ehl contact. Lubricants. 2018;6:80.
12. Hirst W, Moore AJ. Non-newtonian behaviour in elastohydrodynamic lubrication. Proc Royal Soc Lond A Math Phys Sci. 1974;337:101–21.
13. Bauer N, Baumann M, Feldmeth S, Bauer F, Schmitz K. Elastohydrodynamic simulation of pneumatic sealing friction considering 3d surface topography. Chem Eng Technol. 2023;46:167–74.
14. Bauer N, Schmitz K. Influence of manufacturing tolerances on the behavior of pneumatic seals using ehl simulations. Tribol Schmierungstech. 2023;69:62–9.
15. Bauer N, Hahn S, Feldmeth S, Bauer F, Schmitz K. Rheological characterization and ehl simulation of a grease in a lubricated sealing contact. Tribol Schmierungstech. 2021;68:20–8.
16. Angerhausen J, Woyciniuk M, Murrenhoff H, Schmitz K. Simulation and experimental validation of translational hydraulic seal wear. Tribol Int. 2019;134:296–307.
17. Bauer N, Rambaks A, Müller C, Murrenhoff H, Schmitz K. Strategies for implementing the jakobsson-floberg-olsson cavitation model in ehl simulations of translational seals. Int J Fluid Power 2021.
18. Bauer N, Sumbat B, Feldmeth S, Bauer F, Schmitz K. Experimental determination and ehl simulation of transient friction of pneumatic seals in spool valves. Sealing technology—old school and cutting edge: International Sealing Conference: 21st ISC 2022;503–522 .
19. Brumand-Poor F, Bauer N, Plückhahn N, Schmitz K. Fast computation of lubricated contacts: a physics-informed deep learning approach; 2024.
20. Brumand-Poor F, et al. Extrapolation of hydrodynamic pressure in lubricated contacts: a novel multi-case physics-informed neural network framework. Lubricants. 2024;12:122.
21. Brumand-Poor F, Rom M, Plückhahn N, Schmitz K. Physics-informed deep learning for lubricated contacts with surface roughness as parameter 2024.

22. Brumand-Poor F, Barlog F, Plückhahn N, Thebelt M, Schmitz K. Advancing lubrication calculation: a physics-informed neural network framework for transient effects and cavitation phenomena in reciprocating seals 2024.
23. Brumand-Poor F. et al. Physics-informed neural networks for the Reynolds equation with transient cavitation modeling. Lubricants. 2024;12 .
24. Brumand-Poor F, Rom M, Plückhahn N, Schmitz K. Physics-informed deep learning for lubricated contacts with surface roughness as parameter. Tribologie und Schmierungstechnik 2024;71 .
25. Sadegh H, Mehdi AN, Mehdi A. Classification of acoustic emission signals generated from journal bearing at different lubrication conditions based on wavelet analysis in combination with artificial neural network and genetic algorithm. Tribol Int. 2016;95:426–34.
26. Hasan MS, Kordijazi A, Rohatgi PK, Nosonovsky M. Machine learning models of the transition from solid to liquid lubricated friction and wear in aluminum-graphite composites. Tribol Int. 2022;165: 107326.
27. Marian M, et al. Predicting ehl film thickness parameters by machine learning approaches. Friction. 2023;11:992–1013.
28. Kelley J, Schneider V, Poll G, Marian M. Enhancing practical modeling: a neural network approach for locally-resolved prediction of elastohydrodynamic line contacts. Tribol Int. 2024;199: 109988.
29. Kelley J, Schneider V, Marian M, Poll G. A neural network for fast modeling of elastohydrodynamic line contacts (SSRN, 2024).
30. Marian M, Tremmel S. Current trends and applications of machine learning in tribology—a review. Lubricants. 2021;9:86.
31. Marian M, Tremmel S. Physics-informed machine learning—an emerging trend in tribology. Lubricants. 2023;11:463.
32. Almqvist A. Fundamentals of physics-informed neural networks applied to solve the Reynolds boundary value problem. Lubricants. 2021;9:82.
33. Li L, Li Y, Du Q, Liu T, Xie Y. Ref-nets: physics-informed neural network for Reynolds equation of gas bearing. Comput Methods Appl Mech Eng. 2022;391: 114524.
34. Yadav SK, Thakre G. Solution of lubrication problems with deep neural network. In: Dikshit MK, Soni A, Davim JP, editors. Advances in Manufacturing Engineering. Lecture Notes in Mechanical Engineering. Springer Nature Singapore: Singapore; 2023. p. 471–7.
35. Zhao Y, Guo L, Wong PPL. Application of physics-informed neural network in the analysis of hydrodynamic lubrication. Friction. 2023;11:1253–64.
36. Rom M. Physics-informed neural networks for the Reynolds equation with cavitation modeling. Tribol Int. 2023;179: 108141.
37. Cheng Y, et al. Hl-nets: physics-informed neural networks for hydrodynamic lubrication with cavitation. Tribol Int. 2023;188: 108871.
38. Xi Y, Deng J, Li Y. A solution for finite journal bearings by using physics-informed neural networks with both soft and hard constrains. Ind Lubr Tribol. 2023;75:560–7.
39. Xi Y, Deng J, Li Y. A new method to solve the Reynolds equation including mass-conserving cavitation by physics informed neural networks (pinns) with both soft and hard constraints. Friction. 2024.
40. Rimon MTI, et al. (eds). A Design Study of an Elasto-Hydrodynamic Seal for sCO2 Power Cycle by Using Physics Informed Neural Network, Vol. ASME Power Applied R&D 2023 of *ASME Power Conference* 2023.
41. Shutin D, Kazakov Y, Stebakov I, Savin L. Data-driven and physics-informed approaches for improving the performance of dynamic models of fluid film bearings. Tribol Int. 2024;191: 109136.
42. Zhao Y, Wong PPL. A hybrid data-driven approach for the analysis of hydrodynamic lubrication. Proc Inst Mech Eng Part J J Eng Tribol. 2024;238:320–31.
43. Xi Y, Sun R. Inverse problems in hydrodynamics lubrication: parameter identification in the Reynold equation by using physics-informed neural networks. Proc Inst Mech Eng Part J J Eng Tribol. 2024.
44. Patir N, Cheng HS. An average flow model for determining effects of three-dimensional roughness on partial hydrodynamic lubrication. J Lubr Technol. 1978;100:12–7.
45. Patir N, Cheng HS. Application of average flow model to lubrication between rough sliding surfaces. J Lubr Technol. 1979;101:220–9.
46. Woloszynski T, Podsiadlo P, Stachowiak GW. Efficient solution to the cavitation problem in hydrodynamic lubrication. Tribol Lett. 2015;58.
47. Paturi UMR, Palakurthy ST, Reddy NS. The role of machine learning in tribology: a systematic review. Arch Comput Methods Eng. 2023;30:1345–97.
48. Kanai RA, Desavale RG, Chavan SP. Experimental-based fault diagnosis of rolling bearings using artificial neural network. J Tribol 2016;138.
49. Sadık Ünlü B, Durmuş H, Meriç C. Determination of tribological properties at cusn10 alloy journal bearings by experimental and means of artificial neural networks method. Ind Lubr Tribol. 2012;64:258–64.
50. Canbulut F, Yildirim Ş, Sinanoğlu C. Design of an artificial neural network for analysis of frictional power loss of hydrostatic slipper bearings. Tribol Lett. 2004;17:887–99.
51. Hess N, Shang L. Development of a machine learning model for elastohydrodynamic pressure prediction in journal bearings. J Tribol. 2022;144.
52. Velioglu M, Mitsos A, Dahmen M. Physics-informed neural networks (pinns) for modeling dynamic processes based on limited physical knowledge and data. 2023 AIChE Annual Meeting 2023.
53. Psichogios DC, Ungar LH. A hybrid neural network-first principles approach to process modeling. AIChE J. 1992;38:1499–511.
54. Su H-T, Bhat N, Minderman PA, McAvoy TJ. Integrating neural networks with first principles models for dynamic modeling. IFAC Proc Vol. 1992;25:327–32.
55. Kahrs O, Marquardt W. The validity domain of hybrid models and its application in process optimization. Chem Eng Process. 2007;46:1054–66.
56. Nabian MA, Meidani H. Physics-driven regularization of deep neural networks for enhanced engineering design and analysis. J Comput Inf Sci Eng. 2020;20:436.
57. Cybenko G. Approximation by superpositions of a sigmoidal function. Math Control Signals Systems. 1989;2:303–14.

58. Hornik K, Stinchcombe M, White H. Multilayer feedforward networks are universal approximators. Neural Netw. 1989;2:359–66.
59. Lee H, Kang IS. Neural algorithm for solving differential equations. J Comput Phys. 1990;91:110–31.
60. Lagaris IE, Likas A, Fotiadis DI. Artificial neural networks for solving ordinary and partial differential equations. IEEE Trans Neural Netw. 1998;9:987–1000.
61. Owhadi H. Bayesian numerical homogenization. 2014. arXiv:1406.6668.
62. Raissi M, Perdikaris P, Karniadakis GE. Inferring solutions of differential equations using noisy multi-fidelity data. arXiv:1607.04805.
63. Raissi M, Perdikaris P, Karniadakis GE. Machine learning of linear differential equations using gaussian processes. 2017. arXiv:1701.02440.
64. Raissi M, Perdikaris P, Karniadakis GE. Numerical gaussian processes for time-dependent and non-linear partial differential equations. 2017. arXiv:1703.10230.
65. Raissi M, Karniadakis GE. Hidden physics models: machine learning of nonlinear partial differential equations. J Comput Phys. 2018;357:125–41.
66. Cuomo S. et al. Scientific machine learning through physics–informed neural networks: where we are and what's next. J Sci Comput 2022;92 .
67. Raissi M, Perdikaris P, Karniadakis GE. Physics informed deep learning (part i): Data-driven solutions of nonlinear partial differential equations. 2017. arXiv:1711.10561.
68. Raissi M, Perdikaris P, Karniadakis, GE. Physics informed deep learning (part ii): Data-driven discovery of nonlinear partial differential equations. 2017. arXiv:1711.10566.
69. Raissi M, Perdikaris P, Karniadakis GE. Physics-informed neural networks: a deep learning framework for solving forward and inverse problems involving nonlinear partial differential equations. J Comput Phys. 2019;378:686–707.
70. Antonelo EA. et al. Physics-informed neural nets for control of dynamical systems. 2021. arXiv:2104.02556v3.
71. Cai S, Mao Z, Wang Z, Yin M, Karniadakis GE. Physics-informed neural networks (pinns) for fluid mechanics: a review. Acta Mech Sin. 2021;37:1727–38.
72. Ramos DJ, Cunha BZ, Daniel GB. Evaluation of physics-informed neural networks (pinn) in the solution of the Reynolds equation. J Braz Soc Mech Sci Eng. 2023;45.
73. Kim J, Lee K, Lee D, Jin SY, Park N. Dpm: a novel training method for physics-informed neural networks in extrapolation. 2020. arXiv:2012.02681v1.
74. Fesser L, D'Amico-Wong L, Qiu R. Understanding and mitigating extrapolation failures in physics-informed neural networks. arXiv:2306.09478v2.
75. Bonfanti A, Santana R, Ellero M, Gholami B. On the generalization of pinns outside the training domain and the hyperparameters influencing it. 2023. arXiv:2302.07557v2.
76. Bischof R, Kraus M. Multi-objective loss balancing for physics-informed deep learning. 2021. http://rgdoi.net/10.13140/RG.2.2.20057.24169.
77. Tang Y, et al. Physics-informed recurrent neural network for time dynamics in optical resonances. Nat Comput Sci. 2022;2:169–78.
78. Liu F, Li J, Wang L. Pi-lstm: physics-informed long short-term memory network for structural response modeling. Eng Struct. 2023;292: 116500.
79. Ren P, Rao C, Liu Y, Wang J-X, Sun H. Phycrnet: physics-informed convolutional-recurrent network for solving spatiotemporal pdes. Comput Methods Appl Mech Eng. 2022;389: 114399.
80. Zhang R, Liu Y, Sun H. Physics-informed multi-lstm networks for metamodeling of nonlinear structures. Comput Methods Appl Mech Eng. 2020;369: 113226.
81. Zhao L, Ding X, Prakash B. Pinnsformer: a transformer-based framework for physics-informed neural networks; 2023.
82. Oldenburg J, Borowski F, Öner A, Schmitz K-P, Stiehm M. Geometry aware physics informed neural network surrogate for solving navier–stokes equation (gapinn). Adv Model Simul Eng Sci. 2022;9 .
83. Yuan B, Wang H, Heitor A, Chen X. f-picnn: a physics-informed convolutional neural network for partial differential equations with space-time domain. J Comput Phys. 2024;515: 113284.
84. Scarselli F, Gori M, Tsoi AC, Hagenbuchner M, Monfardini G. The graph neural network model. IEEE Trans Neural Netw. 2009;20:61–80.
85. Bronstein MM, Bruna J, LeCun Y, Szlam A, Vandergheynst P. Geometric deep learning: going beyond euclidean data. arXiv:1611.08097v2.
86. Dalton D, Husmeier D, Gao H. Physics-informed graph neural network emulation of soft-tissue mechanics. Comput Methods Appl Mech Eng. 2023;417: 116351.
87. Kumar A, Ridha S, Narahari M, Ilyas SU. Physics-guided deep neural network to characterize non-newtonian fluid flow for optimal use of energy resources. Expert Syst Appl. 2021;183: 115409.
88. Nguyen TNK, Dairay T, Meunier R, Millet C, Mougeot M. Geometry-aware framework for deep energy method: an application to structural mechanics with hyperelastic materials. arXiv:2405.03427v1.

Publisher's Note